

An Autonomous Vision-Based Algorithm for Interplanetary Navigation

Eleonora Andreis ^{*}, Paolo Panicucci [†], and Francesco Topputo [‡]
Polytechnic University of Milan, 20156, Milan, Italy

The surge of deep-space probes makes it unsustainable to navigate them with standard radiometric tracking. Autonomous interplanetary satellites represent a solution to this problem. In this work, a vision-based navigation algorithm is built by combining an orbit determination method with an image processing pipeline suitable for interplanetary transfers of autonomous platforms. To increase the computational efficiency of the algorithm, an extended Kalman filter is selected as state estimator, fed by the positions of the planets extracted from deep-space images. An enhancement of the estimation accuracy is performed by applying an optimal strategy to select the best pair of planets to track. Moreover, a novel analytical measurement model for deep-space navigation is developed providing a first-order approximation of the light-aberration and light-time effects. Algorithm performance is tested on a high-fidelity, Earth–Mars interplanetary transfer, showing the algorithm applicability for deep-space navigation.

I. Introduction

As a new era of deep-space exploration and exploitation is rapidly approaching, the adoption of efficient and sustainable navigation methods becomes increasingly crucial. Traditional ground-based radiometric tracking, while accurate and reliable, heavily depends on limited resources, such as ground stations and flight dynamics teams. This approach is not applicable in the long term to all the spacecraft launched in deep space. There is then an urgent need to enhance the level of navigation autonomy for future interplanetary missions.

Different alternatives enable autonomous navigation capabilities. Among them, the primary ones are autonomous X-ray pulsar-based navigation [1, 2], semi-autonomous radio-based navigation [3], and autonomous vision-based navigation (VBN) [4, 5]. Among these, X-ray navigation requires large detectors and long integration times [6]. One-way radiometric tracking still relies on Earth-based infrastructure. Whereas, VBN is an economical and fully ground-independent solution: it enables determining the probe position by observing the movement of celestial bodies on optical images [6]. VBN stands out as it is

^{*}Ph.D. Candidate, Department of Aerospace Science and Technology, Via La Masa 34, eleonora.andreis@polimi.it

[†]Assistant Professor, Department of Aerospace Science and Technology, Via La Masa 34, paolo.panicucci@polimi.it

[‡]Professor, Department of Aerospace Science and Technology, Via La Masa 34, francesco.topputo@polimi.it, AIAA Senior Member

also compatible with all mission phases toward celestial bodies: cruise [4, 7–9], mid-range [10–13], and close proximity [14], including landing [5, 15]. Consequently, numerous VBN solutions for approach and close proximity have already been developed for various missions. However, VBN algorithms tailored for interplanetary navigation have only undergone onboard testing, with no direct application in probe operations, as evidenced by the validation conducted during the Deep-Space 1 (DS1) mission in 1998 [16]. Nevertheless, the increasing interest in deep-space missions [17], particularly concerning CubeSats [18], is expected to push the adoption of autonomous optical navigation even in far-range scenarios alongside the research in this field. Current research primarily focuses on implementing orbit determination (OD) algorithms to determine the probe state [8, 9, 19–21]. In Karimi and Mortari [19], innovative angles-only Initial Orbit Determination algorithms are developed, whose output is then used within an extended Kalman filter (EKF) embedding light-effects corrections on the planet position in the measurement model. In Franzese et al. [8], the feasibility of the M-ARGO autonomous deep-space navigation experiment is presented over a low thrust trajectory without considering light time correction. In Andreis et al. [9], an OD algorithm suited to be deployed on a miniaturized processor is developed by studying the most promising EKF implementations for onboard applications. Although these works elaborate on autonomy, there is a gap in the literature regarding the development of a fully integrated pipeline embedding an image-processing procedure for extracting information from deep-space images. In Bhaskaran [22], an IP technique to retrieve beacon information is qualitatively mentioned yet not implemented in a fully integrated simulation, and the effect of the measurement errors on the state estimation is not quantified through simulations. Bhaskaran et al. [7] details the procedure adopted to process the deep-space images of DS1. Due to the long exposure time and high-speed slew rate of the mission, complex image patterns were produced for the point sources. Thus, to retrieve accurately the centroids of the bright objects and the beacon position in the image, computationally heavy multiple cross-correlations were applied, following the approach used for the Galileo mission [23]. In this work, an alternative and computationally lighter approach has been preferred based only on geometrical evaluations following the assumptions of having slower slew rates.

To address these literature gaps, this paper develops an autonomous VBN algorithm intended for use during a deep-space transfer, where the estimation accuracy is improved by applying light-effect corrections and an optimal strategy to select the best pair of beacons to track. The contribution to the state-of-the-art is threefold. First, the extended Kalman filter adopted as OD algorithm [9] is integrated with an IP pipeline suited to deep-space navigation [24]. The work in Andreis et al. [9] and Casini et al. [20] is extended by considering synthetic deep-space images as input. In this way, the measurements are the outcome of an IP procedure rather than being simulated with a mere behavioral model. Consequently, they introduce a more authentic representation of the actual measurement error associated with the image processing and real cameras, resulting in a more accurate reproduction of the state estimation error. Second, the VBN filter is

developed for CubeSat applications, thus, particular attention has been paid to the computation capabilities of the navigation algorithm. Third, a novel analytical measurement model for deep-space navigation providing a first-order approximation of light-time correction on beacon position is presented. The proposed model avoids any calculations on the raw camera measurement, so decoupling the spacecraft prediction from the process noise and prevents onboard optimization as in Andreis et al. [9]. Moreover, light-aberration correction is also applied to stars position, being the attitude determined from deep-space images.

The paper is structured as follows. In Sec. II the interplanetary navigation problem is described by paying particular attention to the definition of the optimal beacon selection method and light-effects perturbations relevant in the deep-space environment. Sec. III details the IP procedure to extract observations from deep-space images. In Sec. IV, the developed VBN filter to be used during an interplanetary transfer is presented. Here, the dynamics and measurement models are described together with the chosen filtering scheme. Eventually, the performance of the IP pipeline and the VBN filter tested on an interplanetary high-fidelity ballistic trajectory is reported in Sec. V.

II. Interplanetary Vision-Based Navigation Problem

A. Problem Geometry

A probe can determine its location by acquiring information from the observation of celestial bodies through optical sensors. Since celestial objects are unresolved in deep space (i.e., they fall within a single pixel) their line-of-sight (LoS) direction or pixel position is the only available information that can be used to estimate the probe state. When two LoS directions associated with different beacons are obtained simultaneously, the kinematic celestial triangulation problem can be solved [4, 19, 25].

In this work, CubeSats applications are investigated. This brings us to enforce some constraints, which make the navigation problem even more challenging than for standard probes:

- 1) only one miniaturized optical sensor (e.g., star tracker or camera) is adopted;
- 2) only planets are tracked because of the limited performance of the optical sensor [26];

However, note that the algorithm can be also used for larger spacecraft, despite the examples reported in this paper.

Since to solve the kinematic celestial triangulation problem at least two different synchronous observations are needed, the static celestial triangulation cannot be exploited for the CubeSat operational scenario, given the low probability of detecting several planets with only one instrument. It is worth noting that, in case of a fortunate detection of two planets, the position triangulation would be affected by high uncertainty, given that the two associate LoSes are almost parallel [27]. Therefore, dynamic estimators (e.g., Kalman filtering) are adopted as they can process asynchronous observations and estimate the probe velocity.

B. Optimal Planets Selection

To reach the highest accuracy possible in the state estimation, the approach described in Franzese and Topputo [27] is adopted to optimally select the planets to observe during the interplanetary transfer. The optimal planets pair is chosen among the observable ones by minimizing the figure of merit \mathcal{J} , which is the trace of the position error covariance matrix when considering perturbed LoS directions. It is defined as follows:

$$\mathcal{J} = \sigma_{\text{str}}^2 \frac{1 + \cos \gamma^2}{\sin \gamma^4} \mathbf{d}^\top \left((\mathbf{I}_{3 \times 3} - \hat{\boldsymbol{\rho}}_i \hat{\boldsymbol{\rho}}_i^\top) + (\mathbf{I}_{3 \times 3} - \hat{\boldsymbol{\rho}}_j \hat{\boldsymbol{\rho}}_j^\top) \right) \mathbf{d} \quad (1)$$

where $\hat{\boldsymbol{\rho}}_i$ and $\hat{\boldsymbol{\rho}}_j$ are the unitary LoS vectors to the i -esimal and j -esimal planets, respectively, σ_{str} is the standard deviation of the LoS angular error, and $\mathbf{I}_{3 \times 3}$ is the three-by-three identity matrix. Whereas, \mathbf{d} and γ are defined as

$$\mathbf{d} = \mathbf{r}_i - \mathbf{r}_j \quad (2)$$

$$\gamma = \text{acos}(\hat{\boldsymbol{\rho}}_i^\top \hat{\boldsymbol{\rho}}_j) \quad (3)$$

where \mathbf{r}_i and \mathbf{r}_j are the positions of the two planets in the inertial reference frame, respectively. It is convenient to divide \mathbf{d} by 1 AU to keep \mathcal{J} non-dimensional.

The optimal planet pair is selected taking into account the planets observability, which is preliminarily assessed by evaluating the planet apparent magnitude and Solar Exclusion Angle (SEA). For more information refer to Andreis et al. [9]. In this work, the optimal planet selection procedure is used to choose the two planets to be sequentially targeted in different images, typically containing only one planet at a time.

C. Light-Effects Perturbations

Another important aspect for deep-space navigation is the impact of light effects (i.e., light time and light aberration [19]) on the observations used to estimate the spacecraft state. The light-effect perturbations are caused by two factors. The first one is caused by the large distance between the spacecraft and the beacon involved in deep space and by the finite speed of the light. This implies that the light detected at the camera has been emitted from the source in the past, causing the celestial object to be observed shifted with respect to its position in the instant of detection by the camera. The fastest and further the planet is, the more significant the light-time effect is. For what concerns the second factor, light aberration is a phenomenon where celestial objects display an apparent motion with respect to their true positions relative to the observer velocity. Since the spacecraft velocity is not negligible in deep space, light-aberration effects become important. The location shift of the celestial body depends on the velocity magnitude and direction relative to the LoS of the observed planet.

These two effects shall be corrected in the filter to avoid systematic errors in the estimation of the

spacecraft state. Previous works consider these effects by applying corrections only to the planet LoS directions [9, 19]. Instead, in this work, as the probe attitude is derived from deep-space images, it becomes necessary to apply light aberration correction to the calculated stars LoS directions, as typically done by star trackers [28, 29]. This correction is essential to prevent the computation of a biased attitude value. It is worth noting that only light aberration requires a correction for stars, as they are considered fixed with respect to the Solar System. The corrections of these two effects are described in the upcoming sections.

III. Image Processing Pipeline for Deep-Space Vision-Based Navigation

Let $\mathbb{C} = \{C, C_1, C_2\}$ be the 2D camera reference frame where C_1 points to the right, C_2 downward, and the reference frame center C is placed at the upper left-hand corner of the image. In deep space, the projection of the planet position in \mathbb{C} , called ${}^{\mathbb{C}}r_{pl}$, or its associated LoS direction, is the only information available to support state estimation. An IP algorithm suited for deep-space navigation is adopted to extract this information from the image. The goal of the IP procedure is to recognize the planet locations in the image among the centroids available. The procedure, whose high-level representation is shown in Fig. 1, goes through three steps: 1) The probe attitude is determined, 2) the light-aberration correction is applied to bright star centroids, and 3) the planets are identified. Note that the first step is to identify the portion of the sky the probe is observing and recognize those bright spots that correspond to non-stellar objects in the image. Although the current implementation foresees the attitude determination from the image, note that the Attitude Determination and Control System can also provide this solution in an operative scenario.

A. Attitude Determination

As first step, the probe determines its attitude. To this aim, Niblack's thresholding method [30] is adopted to remove the background noise to patches of the image centered on bright pixels and delimited by squared windows with a one-pixel margin on each side. Hence, the centroid of the object is computed by applying an intensity-weighted center of gravity algorithm considering the pixels inside the associated squared window [31]. Specifically, the intensity-weighted center-of-gravity method has been selected as it presents enhanced accuracy compared to the simple center-of-gravity approach and minor computation effort compared to Gaussian fitting procedures [32], respecting the computational constraint enforced by the CubeSat application.

Then, the registration problem is solved to find the correct matching between the observed star asterism (i.e., stellar pattern) and the cataloged stars in the inertial frame. This last step is performed differently according to whether the planet is acquired for the first time or not.

1. Lost-In-Space Strategy

In the former case, the selected Lost-In-Space (LIS) strategy is the pyramid algorithm detailed in Mortari et al. [33]. In this work, the pyramid algorithm has been preferred over the binary search technique [34] for its higher speed gain rate (from 10 to more than 50 times [35]) and for its robustness to spikes (i.e., objects not recognized as stars by the pyramid algorithm). During the operational phase, the pyramid algorithm accesses the star catalog by exploiting an additional vector of integer stored onboard (i.e., the k-vector) which avoids binary search and makes searching time independent from the database size. Specifically, the interstellar angle is the invariant chosen to build the vector adopted for onboard star identification. To meet the stringent memory constraints of a miniaturized onboard computer, solely angles less than 35 degrees are considered to reduce the catalog size. Additionally, only stars with an apparent magnitude lower than 5.5 are adopted in the generation of the invariant. Moreover, the pyramid feature extraction phase is based on subgraph isomorphism. In other terms, an isomorphic subgraph (in this case a pyramid) corresponding to the measured one has to be found in the onboard database for star identification [36]. Note that the objects identified by the pyramid algorithm as spikes may be non-stellar objects (such as planets, asteroids, and cosmic rays) or stars not recognized due to errors in the centroid extraction. Yet, when a great number of spikes is present in the image, the star asterisms may not be recognized by the algorithm. In this work, to reduce the number of scenarios in which this failure occurs, a heuristic approach is considered. Since faint stars are typically not stored in the onboard catalog and centroids extraction is influenced by the thresholding procedure, the procedure is iterated with an increased intensity threshold if attitude determination fails. This approach has the side effect of reducing the number of bright objects in the image, potentially eliminating some spikes. The iteration continues until observed star asterisms are recognized or fewer than three stars are detected.

2. Recursive Strategy

When the spacecraft is not in LIS mode, it has a rough estimate of its orientation. Therefore, a recursive registration method can be applied. Indeed, by knowing the previous attitude estimation, the LoS directions in the inertial reference frame \mathcal{I} of the four corners of the image are determined. At this point, a check is performed to identify which stars of the onboard catalog are contained inside the image Field of View (FoV). Thus, their locations in the 2D camera reference frame are predicted, and they are associated with the closest centroids of the bright objects extracted from the image when the distances do not exceed a selected threshold value.

When stars are identified, the probe attitude is determined by solving Wahba's problem [37] between the stars' LoS directions in the camera and inertial reference frame exploiting the Singular Value Decomposition (SVD) method [37]. Note the camera reference frame coincides with the body reference frame for the sake of simplicity, while the inertial reference frame is the International Celestial Reference Frame (ICRF). Moreover,

the robustness of the solution to Wahba's problem is increased thanks to the adoption of a RANdom-SAMple Consensus (RANSAC) procedure [38, 39]. The RANSAC algorithm is an outlier rejection method aims to detect the bright objects that have been misidentified by the star identification, which can thus lead to a wrong attitude determination. To detect these outliers, the attitude of the spacecraft is adopted as the mathematical model for the data fitting. The attitude is estimated n_R -times by selecting randomly every time a group of 3 identified stars. A small set of stars needed for attitude determination is chosen to increase the probability of having a group made of different stars at each time. Thus, the estimated n_R spacecraft orientations are compared to identify the best model, which is then adopted for the data fitting. The stars not respecting the best model are considered outliers and are labeled as spikes. When the recursive attitude determination fails, the spacecraft orientation at the following image acquisition is determined again with the LIS method. Conversely, when the LIS algorithm succeeds in the determination of the probe orientation, in the following image acquisition the recursive attitude determination algorithm is adopted.

B. Light-Aberration Correction

After the first attitude determination, the centroids of the stars are corrected for the light-aberration effect, and the probe attitude is recomputed by taking into account the corrected stars LoS directions. The procedure adopted is described in [19] and summarized in this section. At first, the observed stars LoS directions as seen by the spacecraft in the inertial reference frame \mathcal{I} are found:

$${}^{\mathcal{I}}\boldsymbol{\rho}_{s_{\text{obs}}} = (\mathbf{K}_{\text{cam}}\mathbf{A})^{-1}{}^{\mathbb{C}}_h\mathbf{r}_{s_{\text{obs}}} \quad (4)$$

where ${}^{\mathbb{C}}_h\mathbf{r}_{s_{\text{obs}}} = [{}^{\mathbb{C}}\mathbf{r}_{s_{\text{obs}}}; 1]^{\top}$ are the observed stars projection in \mathbb{C} in homogeneous coordinates (see Hartley and Zisserman [39] for homogeneous coordinates definition). Conversely, \mathbf{A} is the attitude matrix, and \mathbf{K}_{cam} is the camera calibration matrix defined as:

$$\mathbf{K}_{\text{cam}} = \begin{bmatrix} f_1 & 0 & c_1 \\ 0 & f_2 & c_2 \\ 0 & 0 & 1 \end{bmatrix} \quad (5)$$

where f_1 and f_2 represent the camera focal length along \mathbf{C}_1 and \mathbf{C}_2 directions in pixel. Whereas, c_1 and c_2 describe the position of the principal point in pixels in \mathbb{C} . Then, the angle θ_{obs} between ${}^{\mathcal{I}}\hat{\boldsymbol{\rho}}_{s_{\text{obs}}}$ (i.e., the unit vector of ${}^{\mathcal{I}}\boldsymbol{\rho}_{s_{\text{obs}}}$) and the estimated unitary velocity vector of the probe $\hat{\mathbf{v}}$ is defined as

$$\tan \theta_{\text{obs}} = \frac{\|{}^{\mathcal{I}}\hat{\boldsymbol{\rho}}_{s_{\text{obs}}} \times \hat{\mathbf{v}}\|}{{}^{\mathcal{I}}\hat{\boldsymbol{\rho}}_{s_{\text{obs}}}^{\top} \hat{\mathbf{v}}} \quad (6)$$

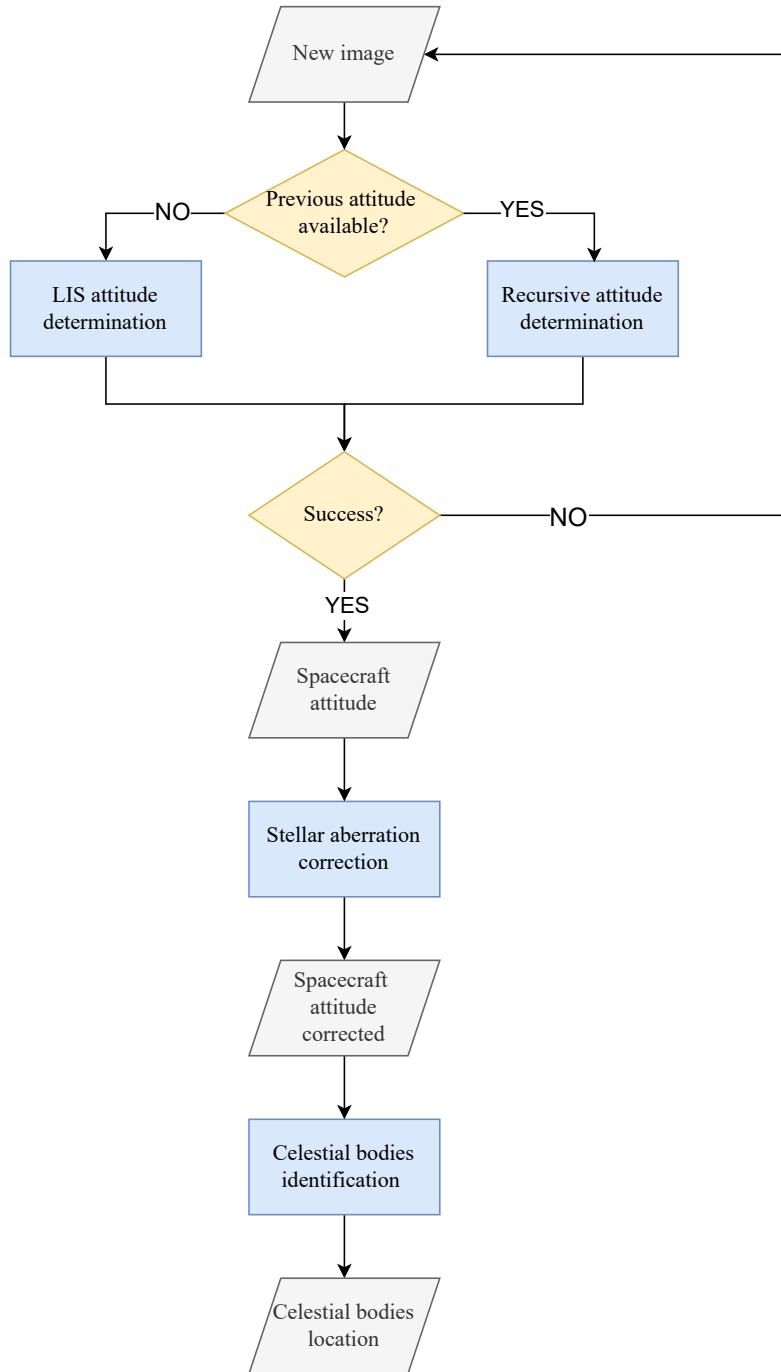


Fig. 1 High-level workflow of the two modes of the image processing procedure

Then the aberration angle ε is evaluated:

$$\tan \varepsilon = \frac{(v/c) \sin \theta_{\text{obs}}}{1 - (v/c) \cos \theta_{\text{obs}}} \quad (7)$$

where c is the speed of light. Thus, the corrected unitary stars LoS directions ${}^T \hat{\rho}_{\text{scorr}}$ can be retrieved as

$${}^I \hat{\boldsymbol{\rho}}_{s_{\text{corr}}} = \frac{{}^I \hat{\boldsymbol{\rho}}_{s_{\text{obs}}} \sin \theta_{\text{corr}} - \hat{\mathbf{v}} \sin \varepsilon}{\sin \theta_{\text{obs}}} \quad (8)$$

with $\theta_{\text{corr}} = \theta_{\text{obs}} + \varepsilon$. At this point, the attitude matrix of the probe is redetermined by solving Wahba's problem [37] in which ${}^I \hat{\boldsymbol{\rho}}_{s_{\text{corr}}}$ are considered. This corrected attitude matrix is labeled \mathbf{A}_{corr} .

C. Beacon Identification

At this step, the planet must be identified in the image and its projection ${}^C \mathbf{r}_{\text{pl}}$ must be extracted. The identification is performed through the evaluation of the mean and covariance matrix associated with the planet location. This latter defines the Gaussian probability of finding the planet in that portion of the image. At first, the expected location of the observed planet in the image plane is evaluated as:

$${}^C_h \mathbf{r}_{\text{pl}_0} = \mathbf{K}_{\text{cam}} \mathbf{A}_{\text{corr}} ({}^I \mathbf{r}_{\text{pl}} - {}^I \mathbf{r}) \quad (9)$$

where ${}^I \mathbf{r}$ is the predicted probe position. If ${}^C_h \mathbf{r}_{\text{pl}_0}$ falls within the boundaries of the image, its associated 3σ covariance ellipse is computed. The latter depends on the uncertainties of the spacecraft pose and planet position and is centered in ${}^C_h \mathbf{r}_{\text{pl}_0}$. The ellipse of ${}^C_h \mathbf{r}_{\text{pl}_0}$ represents the area of the image where the planet is most likely to be found within a 3σ probability. The spike contained in the 3σ ellipse is identified as the planet location ${}^C \mathbf{r}_{\text{pl}}$. If multiple spikes are located within this ellipse, the closest one to the expected planet position is identified as the planet, as it is most likely to be the true planet location. The covariance matrix of the beacon location \mathbf{P} due to the spacecraft pose (i.e., probe attitude and position) and beacon position uncertainty is computed as

$$\mathbf{P} = \mathbf{G} \mathbf{S} \mathbf{G}^T \quad (10)$$

\mathbf{G} is the matrix describing the mapping between ${}^C \mathbf{r}_{\text{pl}}$ and the spacecraft pose and beacon position. \mathbf{S} is the covariance matrix of the probe pose and beacon position. To evaluate \mathbf{G} , the variation of ${}^C \mathbf{r}_{\text{pl}}$ with respect to the variation of the spacecraft pose and the beacon position is computed. In particular, the quaternions $\mathbf{q}_{C/N} = (q_0, \mathbf{q}_v)^T$ are chosen to represent the probe attitude matrix. Specifically, q_0 and \mathbf{q}_v represent the quaternion scalar and vectorial part, respectively. Eq. (11) gives the quaternion representation of the attitude matrix \mathbf{A}_{corr} [37]

$$\mathbf{A}_{\text{corr}} = (q_0^2 - \mathbf{q}_v^T \mathbf{q}_v) \mathbf{I}_{3 \times 3} + 2\mathbf{q}_v \mathbf{q}_v^T - 2q_0 [\mathbf{q}_v]^\wedge \quad (11)$$

where $[(\cdot)]^\wedge$ is the skew-symmetric matrix associated with the cross-product operation. Thus, the variation of ${}^C \mathbf{r}_{\text{pl}}$ with respect to the variation of the spacecraft pose (i.e., \mathbf{A}_{corr} and ${}^I \mathbf{r}$), and the beacon position ${}^I \mathbf{r}_{\text{pl}}$

can be defined as

$$\delta {}^C \mathbf{r}_{\text{pl}} = \underbrace{\begin{bmatrix} \frac{\partial {}^C \mathbf{r}_{\text{pl}}}{\partial q_0} & \left[\frac{\partial {}^C \mathbf{r}_{\text{pl}}}{\partial \mathbf{q}_v} \right] & \left[\frac{\partial {}^C \mathbf{r}_{\text{pl}}}{\partial {}^I \mathbf{r}} \right] & \left[\frac{\partial {}^C \mathbf{r}_{\text{pl}}}{\partial {}^I \mathbf{r}_{\text{pl}}} \right] \end{bmatrix}}_{\mathbf{G}} \begin{pmatrix} \delta q_0 \\ \delta \mathbf{q}_v \\ \delta {}^I \mathbf{r} \\ \delta {}^I \mathbf{r}_{\text{pl}} \end{pmatrix} \quad (12)$$

Here the quaternion $\mathbf{q}_{C/I} = (q_0, \mathbf{q}_v)^\top$ represents the rotation from inertial reference frame I to the camera reference frame C . The matrix \mathbf{G} has dimension 2×10 and it can be expressed as

$$\mathbf{G} = \underbrace{\begin{bmatrix} 1 & 0 & -\frac{{}^C r_{\text{pl},(1)}}{{}^C h_{\text{pl},3}} \\ \frac{{}^C r_{\text{pl},3}}{{}^C h_{\text{pl},3}} & 1 & -\frac{{}^C r_{\text{pl},(2)}}{{}^C h_{\text{pl},3}} \\ 0 & \frac{{}^C r_{\text{pl},(3)}}{{}^C h_{\text{pl},3}} & -\frac{{}^C r_{\text{pl},(1)}}{{}^C h_{\text{pl},3}} \end{bmatrix}}_{\mathbf{D}} \mathbf{K}_{\text{cam}} \begin{bmatrix} \frac{\partial {}^C r_{\text{pl}}}{\partial q_0} & \frac{\partial {}^C r_{\text{pl}}}{\partial \mathbf{q}_v} & \frac{\partial {}^C r_{\text{pl}}}{\partial {}^I \mathbf{r}} & \frac{\partial {}^C r_{\text{pl}}}{\partial {}^I \mathbf{r}_{\text{pl}}} \end{bmatrix} \quad (13)$$

with \mathbf{D} the matrix containing the derivatives of ${}^C \mathbf{r}_{\text{pl}}$ with respect to ${}^C \mathbf{r}_{\text{pl}}$, and ${}^C r_{\text{pl},(i)}$ the i -esimal component of the object location in homogenous coordinates. Note that the partial derivatives of ${}^C \mathbf{r}_{\text{pl}} = \mathbf{A}_{\text{corr}} ({}^I \mathbf{r}_{\text{pl}} - {}^I \mathbf{r})$ with respect to the spacecraft pose and beacon position are

$$\frac{\partial {}^C r_{\text{pl}}}{\partial q_0} = 2q_0 {}^I \boldsymbol{\rho} - 2[\mathbf{q}_v]^\wedge {}^I \boldsymbol{\rho} \quad (14)$$

$$\frac{\partial {}^C r_{\text{pl}}}{\partial \mathbf{q}_v} = -2 {}^I \boldsymbol{\rho} \mathbf{q}_v^\top + 2\mathbf{q}_v^\top {}^I \boldsymbol{\rho} \mathbf{I}_{3 \times 3} + 2\mathbf{q}_v {}^I \boldsymbol{\rho}^\top + 2q_0 [{}^I \boldsymbol{\rho}]^\wedge \quad (15)$$

$$\frac{\partial {}^C r_{\text{pl}}}{\partial {}^I \mathbf{r}} = -\mathbf{A}_{\text{corr}} \quad (16)$$

$$\frac{\partial {}^C r_{\text{pl}}}{\partial {}^I \mathbf{r}_{\text{pl}}} = \mathbf{A}_{\text{corr}} \quad (17)$$

A change of attitude representation is performed to define \mathbf{S} . Since the uncertainty of the probe orientation is more clearly identified through Euler's principal rotation theorem, the quaternion variation is linked to the one relative to the principal angle θ , also known as pointing error, and principal axis \mathbf{e} . Moreover, a reference attitude value is considered to be always present onboard. Therefore, the variation with respect to the nominal value is limited. Thus, the small-error-angles formulation can be adopted [37]:

$$\delta q_0 = 1 \quad (18)$$

$$\delta \mathbf{q}_v = \frac{1}{2} \delta(\theta \mathbf{e}) \quad (19)$$

It is worth noting that the variance of the scalar part is $\sigma_{q_0}^2 = 0$. Therefore, \mathbf{S} can be described:

$$\mathbf{S} = \text{diag}(\sigma_{q_0}^2, \sigma_{q_v}^2 \mathbf{I}_{3 \times 3}, \sigma_r^2 \mathbf{I}_{3 \times 3}, \sigma_{r_{pl}}^2 \mathbf{I}_{3 \times 3}) \quad (20)$$

where σ_r and $\sigma_{r_{pl}}$ represent the standard deviation of the probe position and beacon position, respectively. The cross-correlations are ignored for simplicity, yet in a more general solution, the spacecraft position and orientation could be correlated. Once the covariance matrix of the beacon location is assessed, the associated 3σ covariance ellipse is computed. Let λ_{\max} and λ_{\min} be the largest and smallest eigenvalues of \mathbf{P} , respectively, and \mathbf{v}_{\max} , \mathbf{v}_{\min} their related eigenvectors. Note that \mathbf{P} has only two eigenvalues. The characteristics of the 3σ covariance ellipse can be computed as:

$$a = \sqrt{11.8292 \lambda_{\max}} \quad b = \sqrt{11.8292 \lambda_{\min}} \quad \psi = \arctan\left(\frac{v_{\max_2}}{v_{\max_1}}\right) \quad (21)$$

where a is the 3σ covariance ellipse semimajor axis, b the 3σ covariance ellipse semiminor axis, ψ the 3σ covariance ellipse orientation (i.e., the angle of the largest eigenvector towards the image axis \mathbf{C}_1), and \mathbf{v}_{\max_2} , \mathbf{v}_{\max_1} the eigenvector related to the maximum eigenvalue along \mathbf{C}_2 and \mathbf{C}_1 directions, respectively. Note that the value 11.8292 represents the inverse cumulative distribution function of the chi-square distribution with 2 degrees of freedom at the values in 0.9973 (3σ). Eventually, the beacon is identified with the closest spike to the expected beacon location contained in the 3σ ellipse.

IV. Extended Kalman Filter Based on Planets Observations

In this section, the VBN filter is described. Firstly, the dynamic and measurement models adopted in the VBN filter are detailed. Successively, the chosen filtering scheme is shown. Note that the vectors specified in this section are always defined in the inertial reference frame \mathcal{I} . Thus, the superscript is indicated only for exceptions.

A. Dynamics Model

The dynamics model adopted in this work is an extension of the one described in Andreis et al. [9]. The process state \mathbf{x} is defined as

$$\mathbf{x}(t) = [\mathbf{r}(t), \mathbf{v}(t), \boldsymbol{\eta}(t)]^\top \quad (22)$$

where \mathbf{r} and \mathbf{v} are the inertial probe position and velocity, respectively, and $\boldsymbol{\eta} = [\boldsymbol{\eta}_R, \boldsymbol{\eta}_{SRP}]^\top$ is a vector of Gauss–Markov (GM) processes accounting for unmodeled terms: a 3-dimensional residual accelerations $\boldsymbol{\eta}_R$ and the stochastic component of the Solar Radiation Pressure (SRP) $\boldsymbol{\eta}_{SRP}$ [40]. The process is modeled using

the following differential equation

$$\dot{\mathbf{x}}(t) = \mathbf{f}(\mathbf{x}(t), t) + \mathbf{w} \quad (23)$$

where \mathbf{f} is the vector field embedding the deterministic part, while \mathbf{w} is the process white noise:

$$\dot{\mathbf{x}}(t) = \underbrace{\begin{bmatrix} \mathbf{v} \\ \mathbf{a}_{\text{Sun}} + \mathbf{a}_{\text{SRP}} + \sum_i \mathbf{a}_{\text{pl}_i} + \boldsymbol{\eta}_{\text{R}} + \boldsymbol{\eta}_{\text{SRP}} \\ -\xi_{\text{R}}\boldsymbol{\eta}_{\text{R}} \\ -\xi_{\text{SRP}}\boldsymbol{\eta}_{\text{SRP}} \end{bmatrix}}_{\mathbf{f}} + \underbrace{\begin{bmatrix} \mathbf{0}_{3 \times 1} \\ \mathbf{0}_{3 \times 1} \\ \mathbf{w}_{\text{R}} \\ \mathbf{w}_{\text{SRP}} \end{bmatrix}}_{\mathbf{w}} \quad (24)$$

and

$$\mathbf{a}_{\text{Sun}} = -\mu_{\text{Sun}} \frac{\mathbf{r}}{\|\mathbf{r}\|^3} \quad (25)$$

$$\mathbf{a}_{\text{SRP}} = C_{\text{R}} \frac{P_0 R_0^2 A_s}{c m_s} \frac{\mathbf{r}}{\|\mathbf{r}\|^3} \quad (26)$$

$$\mathbf{a}_{\text{pl}_i} = \mu_{\text{pl}_i} \left(\frac{\mathbf{r}_{\text{pl}_i} - \mathbf{r}}{\|\mathbf{r}_{\text{pl}_i} - \mathbf{r}\|^3} - \frac{\mathbf{r}_{\text{pl}_i}}{\|\mathbf{r}_{\text{pl}_i}\|^3} \right) \quad (27)$$

As detailed in Jean et al. [41], the terms that describe the SRP are: C_{R} the coefficient of reflection, P_0 the solar power, R_0 the Sun radius, A_s the cross-section area of the probe, and m_s its mass. The third-body perturbations of the Earth-Moon barycenter, Mars, and Jupiter are also included. Recall that μ_{pl_i} is the gravitational parameter of the i -esimal planet considered. In the Langevin equations that govern the Gauss-Markov processes the coefficients ξ_{R} and ξ_{SRP} define the reciprocal of the correlation times, while \mathbf{w}_{R} and \mathbf{w}_{SRP} are the process noises of the Gauss-Markov parameters with σ_{R} and σ_{SRP} standard deviations. The covariance of these two process noises can be defined as

$$\mathbb{E}[\mathbf{w}_{\text{R}}\mathbf{w}_{\text{R}}^{\top}] = \sigma_{\text{R}}^2 \mathbf{I}_{3 \times 3} = \mathbf{Q}_{\text{R}} \quad \mathbb{E}[\mathbf{w}_{\text{SRP}}\mathbf{w}_{\text{SRP}}^{\top}] = \sigma_{\text{SRP}}^2 \mathbf{I}_{3 \times 3} = \mathbf{Q}_{\text{SRP}} \quad (28)$$

$$(29)$$

These covariances are not a priori known. Yet, reference values for the acceleration uncertainties \mathbf{Q}_{aR} and \mathbf{Q}_{aSRP} are reported in the literature. Moreover, these covariances \mathbf{Q}_{aR} and \mathbf{Q}_{aSRP} can be treated as steady-state covariance values of the GM parameters [40]. That is,

$$\mathbb{E}[\boldsymbol{\eta}_{\text{R}}\boldsymbol{\eta}_{\text{R}}^{\top}] = \frac{\mathbf{Q}_{\text{R}}}{2\xi_{\text{R}}} = \mathbf{Q}_{\text{aR}} \quad \mathbb{E}[\boldsymbol{\eta}_{\text{SRP}}\boldsymbol{\eta}_{\text{SRP}}^{\top}] = \frac{\mathbf{Q}_{\text{SRP}}}{2\xi_{\text{SRP}}} = \mathbf{Q}_{\text{aSRP}} \quad (30)$$

From which \mathbf{Q}_{SRP} and \mathbf{Q}_{R} can be computed. The complete process noise covariance matrix is \mathbf{Q} :

$$\mathbf{Q} = \text{diag}(0_{3 \times 3}, 0_{3 \times 3}, \mathbf{Q}_{\text{R}}, \mathbf{Q}_{\text{SRP}}) \quad (31)$$

B. Measurement Model

One of the contributions of the work is to present a novel measurement model for deep-space triangulation. The exploited measurement model expresses the position of the observations in pixel coordinates in the camera reference frame \mathbb{C} . Moreover, it embeds the light effects and their dependencies, which are described with respect to the planet and spacecraft state.

In the existing literature, external observations are frequently modeled as LoS directions or angular coordinates, such as azimuth and elevation [8, 19, 42]. This conventional approach involves manipulating raw camera measurements (i.e., pixel coordinates), resulting in a non-Gaussian error distribution compared to the original raw data. Moreover, prior studies have attempted non-linear correction of light-aberration effects on the observations by employing the a priori estimate of velocity. However, this method couples measurement and process noise, thus violating the Kalman filter assumption [9, 19]. Furthermore, light-time delay is typically evaluated in the literature using an iterative approach, which increases the computational time required to achieve an optimal solution.

In contrast, the developed measurement model utilizes pixel coordinates to represent observations and incorporates light effects within the model itself to enhance correlations and improve linearity, thus avoiding coupling between measurement and process noises. Eventually, the light-time delay is derived through a linear approximation of the equation describing the light-time effect.

1. Evaluation of the time delay

To proceed with the implementation of the light-time correction, it is first necessary to evaluate the time delay Δt . As the initial step, the equation representing the light-time effect can be written as follows [9]:

$$\mathfrak{L} := c^2 (t - \tau)^2 - (\mathbf{r}_{\text{pl}}(\tau) - \mathbf{r}(t))^{\top} (\mathbf{r}_{\text{pl}}(\tau) - \mathbf{r}(t)) = 0 \quad (32)$$

where τ is the time at which the light is emitted by the planet and t is the time of measurement.

Eq. (32) is a constraint that links the spacecraft state with the planet position. Moreover, as the planet motion does not have an analytical solution, the value of τ cannot be solved analytically to implicitly include this effect in the measurement. Yet, it is possible to linearize the constraint in Eq. (32) with respect to Δt under the assumption that the time delay $\Delta t = t - \tau$ is small with respect to the orbital period. Thus, the

planet motion can be approximated by a linear motion with constant velocity as follows:

$$\mathbf{r}_{\text{pl}}(\tau) \simeq \mathbf{r}_{\text{pl}}(t) + \left. \frac{d\mathbf{r}_{\text{pl}}}{d\tau} \right|_{\tau=t} (\tau - t) = \mathbf{r}_{\text{pl}}(t) - \left. \frac{d\mathbf{r}_{\text{pl}}}{d\tau} \right|_{\tau=t} \Delta t = \mathbf{r}_{\text{pl}}(t) - \mathbf{v}_{\text{pl}}(t) \Delta t \quad (33)$$

Therefore, Eq. (32) can be linearized as well as follows:

$$\begin{aligned} \mathfrak{L} &\simeq c^2 \Delta t^2 - (\mathbf{r}_{\text{pl}}(t) - \mathbf{v}_{\text{pl}}(t) \Delta t - \mathbf{r}(t))^\top (\mathbf{r}_{\text{pl}}(t) - \mathbf{v}_{\text{pl}}(t) \Delta t - \mathbf{r}(t)) \\ &= (c^2 - \mathbf{v}_{\text{pl}}(t)^\top \mathbf{v}_{\text{pl}}(t)) \Delta t^2 + 2\mathbf{v}_{\text{pl}}(t)^\top \mathbf{r}_{\text{pl}/\text{sc}}(t) \Delta t - \mathbf{r}_{\text{pl}/\text{sc}}(t)^\top \mathbf{r}_{\text{pl}/\text{sc}}(t) \end{aligned} \quad (34)$$

where $\mathbf{r}_{\text{pl}/\text{sc}}(t) = \mathbf{r}_{\text{pl}}(t) - \mathbf{r}(t)$. Thus, the solution Δt is obtained by solving a second-order polynomial equation:

$$\begin{aligned} \Delta t &= \frac{1}{c^2 - \mathbf{v}_{\text{pl}}(t)^\top \mathbf{v}_{\text{pl}}(t)} \left(-\mathbf{r}_{\text{pl}/\text{sc}}(t)^\top \mathbf{v}_{\text{pl}}(t) \right. \\ &\quad \left. \pm \sqrt{\mathbf{r}_{\text{pl}/\text{sc}}(t)^\top \mathbf{r}_{\text{pl}/\text{sc}}(t) (c^2 - \mathbf{v}_{\text{pl}}(t)^\top \mathbf{v}_{\text{pl}}(t)) + (\mathbf{r}_{\text{pl}/\text{sc}}(t)^\top \mathbf{v}_{\text{pl}}(t))^2} \right) \end{aligned} \quad (35)$$

Eq. (35) shows that two solutions are possible, given the geometry between the planet and the spacecraft. It is important to understand which solution is the correct one to uniquely solve for Δt . By defining $\boldsymbol{\beta}_{\text{pl}}(t) = \frac{\mathbf{v}_{\text{pl}}(t)}{c}$ and the angle between $\mathbf{r}_{\text{pl}/\text{sc}}(t)$ and $\mathbf{v}_{\text{pl}}(t)$ as the planet flight path angle ϵ , the approximated solution for the light-time correction is:

$$\Delta t = \frac{-c \|\mathbf{r}_{\text{pl}/\text{sc}}(t)\| \|\boldsymbol{\beta}_{\text{pl}}(t)\| \cos \epsilon \pm c \|\mathbf{r}_{\text{pl}/\text{sc}}(t)\| \sqrt{\|\boldsymbol{\beta}_{\text{pl}}(t)\|^2 (\cos^2 \epsilon - 1) + 1}}{c^2 (1 - \|\boldsymbol{\beta}_{\text{pl}}(t)\|^2)} \quad (36)$$

Recall that the correct solution is the one providing $\Delta t \geq 0$ as the light departs from the planet before arriving at the spacecraft camera. As a consequence, the solution with the plus sign is the one providing the correct time delay. Thus:

$$\Delta t = \frac{\|\mathbf{r}_{\text{pl}/\text{sc}}(t)\|}{c (1 - \|\boldsymbol{\beta}_{\text{pl}}(t)\|^2)} \left(-\|\boldsymbol{\beta}_{\text{pl}}(t)\| \cos \epsilon + \sqrt{\|\boldsymbol{\beta}_{\text{pl}}(t)\|^2 (\cos^2 \epsilon - 1) + 1} \right) \quad (37)$$

Since $\|\boldsymbol{\beta}_{\text{pl}}(t)\| \leq 1$, $1 - \|\boldsymbol{\beta}_{\text{pl}}(t)\|^2 \geq 0 \forall \boldsymbol{\beta}_{\text{pl}}(t)$ and $\|\boldsymbol{\beta}_{\text{pl}}(t)\|^2 (\cos^2 \epsilon - 1) + 1 \geq 0 \forall \boldsymbol{\beta}_{\text{pl}}(t)$ and $\forall \epsilon$. Note that $\cos \epsilon \geq 0 \forall \epsilon$ by flight path angle definition. Eq. (37) provides an analytical solution at first order for the light-time delay which can be exploited to include light-time correction in the filter update.

2. Definition of the measurement model equation

Once Δt is computed, the planet LoS can be expressed as the unit vector for the spacecraft position at time t to the planet position at time τ . Thus:

$$\mathbf{l}_{\text{pl/sc}} = \frac{\mathbf{r}_{\text{pl}}(t - \Delta t) - \mathbf{r}(t)}{\left\| (\mathbf{r}_{\text{pl}}(t - \Delta t) - \mathbf{r}(t))^\top (\mathbf{r}_{\text{pl}}(t - \Delta t) - \mathbf{r}(t)) \right\|} \quad (38)$$

This unit vector is warped by relativistic light aberration as the spacecraft is not fixed with respect to the inertial reference frame. At first order, this effect can be expressed as follows [43]:

$$\mathbf{l}_{\text{pl/sc}}^{\text{aberr}} = \mathbf{l}_{\text{pl/sc}} + \mathbf{l}_{\text{pl/sc}} \times (\boldsymbol{\beta}_{\text{sc}} \times \mathbf{l}_{\text{pl/sc}}) \quad (39)$$

where $\boldsymbol{\beta}_{\text{sc}} = \frac{\mathbf{v}}{c}$. Note that higher orders are not detectable from the image processing pipeline as they are orders of magnitude below 15 arcsec [44], which is attitude determination performance.

Finally, the warped line of sight is projected in the camera:

$${}^{\text{C}}_h \mathbf{r}_{\text{pl}} = \mathbf{K}_{\text{cam}} \mathbf{A}_{\text{corr}} \mathbf{l}_{\text{pl/sc}}^{\text{aberr}} \quad (40)$$

$${}^{\text{C}} \mathbf{r}_{\text{pl}} = \frac{1}{{}^{\text{C}}_h r_{\text{pl},(3)}} \begin{pmatrix} {}^{\text{C}}_h r_{\text{pl},(1)} \\ {}^{\text{C}}_h r_{\text{pl},(2)} \end{pmatrix} \quad (41)$$

where ${}^{\text{C}}_h \mathbf{r}_{\text{pl}}$ is the projection of the planet line of sight in the image plane in homogeneous coordinates, ${}^{\text{C}} \mathbf{r}_{\text{pl}}$ represents the planet location in pixel coordinates, ${}^{\text{C}}_h r_{\text{pl},(i)}$ is the i -esimal coordinate of vector ${}^{\text{C}}_h \mathbf{r}_{\text{pl}}$, \mathbf{K}_{cam} is the camera intrinsic matrix, and \mathbf{A}_{corr} is the rotation matrix corrected for the stars light aberration from the inertial reference frame \mathcal{I} to the camera reference frame \mathcal{C} .

3. Definition of the Jacobian of the measurement model

In this section the measurement model derivatives with respect to the filter state and all other possible sources of errors are computed by variational analysis. The considered error sources include the spacecraft attitude and planet state. Once variations are computed, it is possible to use the derivatives with respect to the state to construct the measurement model Jacobian matrix. Moreover, by using the derivatives of the measurement with respect to the other error sources, it is possible to inflate the measurement covariance matrix to account for uncertainties in the spacecraft attitude and planet ephemerides.

To perform the variational analysis, the variation of each parameter is considered, and its nonlinear mapping is approximated with a linear function leveraging its first derivatives. This leads to determining the mapping between the variation of the output parameter with respect to the variation of the parameters under analysis.

Note that $\delta(\cdot)$ is the variation of the considered parameter. Thus:

$$\delta^{\mathbb{C}} \mathbf{r}_{\text{pl}} = \begin{bmatrix} 1 & 0 & -\frac{\mathbb{C} \mathbf{r}_{\text{pl},(1)}}{h \mathbf{r}_{\text{pl},(3)}} \\ \frac{\mathbb{C} \mathbf{r}_{\text{pl},(3)}}{h \mathbf{r}_{\text{pl},(3)}} & 0 & -\frac{\mathbb{C} \mathbf{r}_{\text{pl},(2)}}{h \mathbf{r}_{\text{pl},(3)}} \\ 0 & \frac{1}{h \mathbf{r}_{\text{pl},(3)}} & -\frac{\mathbb{C} \mathbf{r}_{\text{pl},(2)}}{h \mathbf{r}_{\text{pl},(3)}} \end{bmatrix} \delta_h^{\mathbb{C}} \mathbf{r}_{\text{pl}} \quad (42)$$

$$\delta_h^{\mathbb{C}} \mathbf{r}_{\text{pl}} = \mathbf{K}_{\text{cam}} \mathbf{A}_{\text{corr}} \left(\delta \mathbf{l}_{\text{pl}/\text{sc}}^{\text{aberr}} + 2 \left[\mathbf{l}_{\text{pl}/\text{sc}}^{\text{aberr}} \right]^{\wedge} \delta \mathbf{q}_v \right) \quad (43)$$

where \mathbf{q}_v is the vectorial part of the quaternion $\mathbf{q}_{C/I}$ representing the rotation from the inertial reference frame \mathcal{I} to the camera reference frame \mathcal{C} .

The variation of the aberrated line of sight $\mathbf{l}_{\text{pl}/\text{sc}}^{\text{aberr}}$ is computed by exploiting the triple vector product identity $\mathbf{a} \times (\mathbf{b} \times \mathbf{c}) = (\mathbf{a} \cdot \mathbf{c})\mathbf{b} - (\mathbf{a} \cdot \mathbf{b})\mathbf{c}$:

$$\begin{aligned} \delta \mathbf{l}_{\text{pl}/\text{sc}}^{\text{aberr}} = & \left(\mathbf{I}_{3 \times 3} + 2 \boldsymbol{\beta}_{\text{sc}} \mathbf{l}_{\text{pl}/\text{sc}}^{\text{T}} - \mathbf{l}_{\text{pl}/\text{sc}}^{\text{T}} \boldsymbol{\beta}_{\text{sc}} \mathbf{I}_{3 \times 3} - \mathbf{l}_{\text{pl}/\text{sc}} \boldsymbol{\beta}_{\text{sc}}^{\text{T}} \right) \delta \mathbf{l}_{\text{pl}/\text{sc}} + \\ & + \left(\mathbf{l}_{\text{pl}/\text{sc}}^{\text{T}} \mathbf{l}_{\text{pl}/\text{sc}} \mathbf{I}_{3 \times 3} - \mathbf{l}_{\text{pl}/\text{sc}} \mathbf{l}_{\text{pl}/\text{sc}}^{\text{T}} \right) \delta \boldsymbol{\beta}_{\text{sc}} \end{aligned} \quad (44)$$

where $\delta \boldsymbol{\beta}_{\text{sc}} = \frac{\delta \mathbf{v}}{c}$ and $\delta \mathbf{l}_{\text{pl}/\text{sc}}$ is:

$$\begin{aligned} \delta \mathbf{l}_{\text{pl}/\text{sc}} = & \left(\frac{\mathbf{I}_{3 \times 3}}{\left\| \left(\mathbf{r}_{\text{pl}}(t - \Delta t) - \mathbf{r}(t) \right)^{\text{T}} \left(\mathbf{r}_{\text{pl}}(t - \Delta t) - \mathbf{r}(t) \right) \right\|} + \right. \\ & \left. - \frac{\left(\mathbf{r}_{\text{pl}}(t - \Delta t) - \mathbf{r}(t) \right) \left(\mathbf{r}_{\text{pl}}(t - \Delta t) - \mathbf{r}(t) \right)^{\text{T}}}{\left\| \left(\mathbf{r}_{\text{pl}}(t - \Delta t) - \mathbf{r}(t) \right)^{\text{T}} \left(\mathbf{r}_{\text{pl}}(t - \Delta t) - \mathbf{r}(t) \right) \right\|^3} \right) \left(\delta \mathbf{r}_{\text{pl}}(t - \Delta t) - \delta \mathbf{r}(t) \right) \end{aligned} \quad (45)$$

The variation of the observed LoS from the camera can be gathered as follows:

$$\delta \mathbf{r}_{\text{pl}}(t - \Delta t) = \delta \mathbf{r}_{\text{pl}}(t) - \Delta t \delta \mathbf{v}_{\text{pl}}(t) - \mathbf{v}_{\text{pl}}(t) \delta \Delta t \quad (46)$$

where

$$\begin{aligned} \delta \Delta t = & \frac{1}{c^2 - \mathbf{v}_{\text{pl}}(t)^{\text{T}} \mathbf{v}_{\text{pl}}(t)} \left(\left(\frac{(c^2 - \mathbf{v}_{\text{pl}}(t)^{\text{T}} \mathbf{v}_{\text{pl}}(t)) \mathbf{r}_{\text{pl}/\text{sc}}(t)^{\text{T}} + \mathbf{r}_{\text{pl}/\text{sc}}(t)^{\text{T}} \mathbf{v}_{\text{pl}}(t) \mathbf{v}_{\text{pl}}(t)^{\text{T}}}{\sqrt{\mathbf{r}_{\text{pl}/\text{sc}}(t)^{\text{T}} \mathbf{r}_{\text{pl}/\text{sc}}(t) (c^2 - \mathbf{v}_{\text{pl}}(t)^{\text{T}} \mathbf{v}_{\text{pl}}(t)) + (\mathbf{r}_{\text{pl}/\text{sc}}(t)^{\text{T}} \mathbf{v}_{\text{pl}}(t))^2}} \right. \right. \\ & \left. \left. - \mathbf{v}_{\text{pl}}^{\text{T}}(t) \right) \left(\delta \mathbf{r}_{\text{pl}}(t) - \delta \mathbf{r}(t) \right) + \left(\frac{\mathbf{r}_{\text{pl}/\text{sc}}(t)^{\text{T}} \mathbf{v}_{\text{pl}}(t) \mathbf{r}_{\text{pl}/\text{sc}}(t)^{\text{T}} - \mathbf{r}_{\text{pl}/\text{sc}}(t)^{\text{T}} \mathbf{r}_{\text{pl}/\text{sc}}(t) \mathbf{v}_{\text{pl}}(t)^{\text{T}}}{\sqrt{\mathbf{r}_{\text{pl}/\text{sc}}(t)^{\text{T}} \mathbf{r}_{\text{pl}/\text{sc}}(t) (c^2 - \mathbf{v}_{\text{pl}}(t)^{\text{T}} \mathbf{v}_{\text{pl}}(t)) + (\mathbf{r}_{\text{pl}/\text{sc}}(t)^{\text{T}} \mathbf{v}_{\text{pl}}(t))^2}} \right. \right. \\ & \left. \left. + \frac{2 \mathbf{v}_{\text{pl}}(t)^{\text{T}}}{c^2 - \mathbf{v}_{\text{pl}}(t)^{\text{T}} \mathbf{v}_{\text{pl}}(t)} - \mathbf{r}_{\text{pl}/\text{sc}}(t)^{\text{T}} \right) \delta \mathbf{v}_{\text{pl}}(t) \right) \end{aligned} \quad (47)$$

Finally, by combining Eqs. (42)–(47), the linear mapping between the variation of ${}^C\mathbf{r}_{\text{pl}}$ and the variation of \mathbf{r}_{pl} , \mathbf{v}_{pl} , \mathbf{r} , and \mathbf{q}_v can be established:

$$\delta {}^C\mathbf{r}_{\text{pl}} = \begin{bmatrix} \frac{\partial {}^C\mathbf{r}_{\text{pl}}}{\partial \mathbf{r}(t)} & \frac{\partial {}^C\mathbf{r}_{\text{pl}}}{\partial \mathbf{v}(t)} & \frac{\partial {}^C\mathbf{r}_{\text{pl}}}{\partial \mathbf{q}_v} & \frac{\partial {}^C\mathbf{r}_{\text{pl}}}{\partial \mathbf{r}_{\text{pl}}(t)} & \frac{\partial {}^C\mathbf{r}_{\text{pl}}}{\partial \mathbf{v}_{\text{pl}}(t)} \end{bmatrix} \begin{pmatrix} \delta \mathbf{r}(t) \\ \delta \mathbf{v}(t) \\ \delta \mathbf{q}_v \\ \delta \mathbf{r}_{\text{pl}}(t) \\ \delta \mathbf{v}_{\text{pl}}(t) \end{pmatrix} = \begin{bmatrix} 1 & 0 & \frac{{}^C\mathbf{h}\mathbf{r}_{\text{pl},(1)}}{{}^C\mathbf{h}\mathbf{r}_{\text{pl},(3)}^2} \\ \frac{{}^C\mathbf{h}\mathbf{r}_{\text{pl},(3)}}{{}^C\mathbf{h}\mathbf{r}_{\text{pl},(3)}} & & \frac{{}^C\mathbf{h}\mathbf{r}_{\text{pl},(2)}}{{}^C\mathbf{h}\mathbf{r}_{\text{pl},(3)}} \\ 0 & 1 & \frac{{}^C\mathbf{h}\mathbf{r}_{\text{pl},(2)}}{{}^C\mathbf{h}\mathbf{r}_{\text{pl},(3)}} \end{bmatrix} \mathbf{K}_{\text{cam}} \mathbf{A}_{\text{corr}} \begin{bmatrix} \mathbf{R}_{\text{sc}} & \mathbf{V}_{\text{sc}} & \mathbf{Q}_{\text{att}} & \mathbf{R}_{\text{pl}} & \mathbf{V}_{\text{pl}} \end{bmatrix} \begin{pmatrix} \delta \mathbf{r}(t) \\ \delta \mathbf{v}(t) \\ \delta \mathbf{q}_v \\ \delta \mathbf{r}_{\text{pl}}(t) \\ \delta \mathbf{v}_{\text{pl}}(t) \end{pmatrix} \quad (48)$$

where matrices \mathbf{R}_{sc} , \mathbf{V}_{sc} , \mathbf{Q}_{att} , \mathbf{R}_{pl} , and \mathbf{V}_{pl} are reported in Appendix A.

Eq. (48) provides the linear mapping between the projection of the planet in the image plane as a function of the spacecraft state, the spacecraft inertial attitude, and planet ephemeris. Note that matrices $\frac{\partial {}^C\mathbf{r}_{\text{pl}}}{\partial \mathbf{r}(t)}$ and $\frac{\partial {}^C\mathbf{r}_{\text{pl}}}{\partial \mathbf{v}(t)}$ are used to build the measurement model Jacobian \mathbf{H} employed in the Extended Kalman Filter. Moreover, $\frac{\partial {}^C\mathbf{r}_{\text{pl}}}{\partial \mathbf{q}_v}$, $\frac{\partial {}^C\mathbf{r}_{\text{pl}}}{\partial \mathbf{r}_{\text{pl}}(t)}$, and $\frac{\partial {}^C\mathbf{r}_{\text{pl}}}{\partial \mathbf{v}_{\text{pl}}(t)}$ may be used to inflate the measurement covariance matrix taking into account attitude determination uncertainty from the attitude filter and the planet ephemeris uncertainties induced by an onboard implementation of the planet motion.

Note that the advantages of the proposed measurement model are threefold. First, the centroid measurement from the camera raw image is directly provided to the filter without any calculation. Indeed, any operation could increase the non-linearity of the measurement error distribution, leading to less linear behavior of the filter posterior estimates. This is particularly true when trigonometric functions are used as in previous work [9, 19]. Second, the expression found in Eq. (37) is analytic, leading that no optimization is necessary on board to compute the light time delay. This is in contrast with state-of-the-art techniques that use Newton-Raphson's method to find the light-time correction [9, 19, 45]. Third, as the light time correction is embedded in the measurement model, uncertainties arising from the planets ephemeris and correlations with spacecraft state can be taken into account as shown in Eq. (48).

When only light-time correction is included in the measurement model (as in Section V for comparison

analysis), Eqs. (39) and (44) are not used and Eqs. (40) and (43) simply become:

$${}^C_h \mathbf{r}_{pl} = \mathbf{K}_{\text{cam}} \mathbf{A}_{\text{corr}} \mathbf{I}_{pl/sc} \quad (49)$$

$$\delta {}^C_h \mathbf{r}_{pl} = \mathbf{K}_{\text{cam}} \mathbf{A}_{\text{corr}} \left(\delta \mathbf{I}_{pl/sc} + 2 [\mathbf{I}_{pl/sc}]^{\wedge} \delta \mathbf{q}_v \right) \quad (50)$$

C. Selected Filtering Strategy for the Vision-Based Navigation Algorithm

A non-dimensionalized EKF is selected as the most appropriate filtering approach for the development of a VBN algorithm for CubeSat applications. The selection has been performed in Andreis et al. [9], where the behavior of five different EKFs is analyzed in terms of estimator numerical stability and computational performance. Indeed, it is worth recalling that the autonomous VBN algorithm has to be deployed on a miniaturized processor characterized by limited computation capabilities comparable to the one of a Raspberry Pi*. The implemented scheme is reported in Table 1, where all the terms are already non-dimensionalized following the approach discussed in Andreis et al. [9].

Table 1 Filtering strategy

System State Space	$\dot{\mathbf{x}} = \mathbf{f}(\mathbf{x}(t), t) + \mathbf{w}$ $\mathbf{y}_k = \mathbf{h}(\mathbf{x}_k) + \mathbf{v}_k$ $\dot{\mathbf{P}} = \mathbf{F}\mathbf{P} + \mathbf{P}\mathbf{F}^{\top} + \mathbf{Q}$	
Propagation Block	$\mathbf{x}_{pk} = \mathbf{x}_{c_{k-1}} + \int_{t_{k-1}}^{t_k} \mathbf{f}(\mathbf{x}(t), t) dt$ $\mathbf{P}_{pk} = \mathbf{P}_{c_{k-1}} + \int_{t_{k-1}}^{t_k} \dot{\mathbf{P}} dt$	$\mathbf{x}_{c_0} = E[\mathbf{x}_0]$ $\mathbf{P}_{c_0} = E[\mathbf{x}_0 \mathbf{x}_0^{\top}]$
Correction Block	$\mathbf{K}_k = \mathbf{P}_{pk} \mathbf{H}_k^{\top} (\mathbf{H}_k \mathbf{P}_{pk} \mathbf{H}_k^{\top} + \mathbf{R}_k)^{-1}$ $\mathbf{x}_{c_k} = \mathbf{x}_{pk} + \mathbf{K}_k [\mathbf{y}_k - \mathbf{h}(\mathbf{x}_{pk})]$ $\mathbf{P}_{c_k} = (\mathbf{I} - \mathbf{K}_k \mathbf{H}_k) \mathbf{P}_{pk} (\mathbf{I} - \mathbf{K}_k \mathbf{H}_k)^{\top} + \mathbf{K}_k \mathbf{R}_k \mathbf{K}_k^{\top}$	

Recall that \mathbf{x}_{pk} is the predicted state vector with error covariance matrix \mathbf{P}_{pk} at epoch k , \mathbf{K}_k the Kalman gain, \mathbf{x}_{c_k} the corrected state vector with error covariance matrix \mathbf{P}_{c_k} , \mathbf{F} the Jacobian of the dynamics model equation, \mathbf{h} the measurement model equation with Jacobian \mathbf{H}_k , \mathbf{v}_k the measurement white noise, and \mathbf{y}_k is the external measurement vector \mathbf{r}_{pl_k} .

*<https://www.raspberrypi.com/products/raspberry-pi-4-model-b/>, Last Visited on January 2024

The initial probe state vector is perturbed by applying the 3σ standard deviation rule:

$$\mathbf{x}_0 = \tilde{\mathbf{x}}_0 + 3\sqrt{\mathbf{P}_0}\mathbf{k} \quad (51)$$

where $\tilde{\mathbf{x}}_0$ is the probe nominal state, \mathbf{k} is a random scalar drawn from the standard distribution. The square root operates on the elements of the initial error covariance matrix \mathbf{P}_0 , which is defined as:

$$\mathbf{P}_0 = \text{diag}(\sigma_r^2 \mathbf{I}_{3 \times 3}, \sigma_v^2 \mathbf{I}_{3 \times 3}, \sigma_{\eta_R}^2 \mathbf{I}_{3 \times 3}, \sigma_{\eta_{SRP}}^2 \mathbf{I}_{3 \times 3}) \quad (52)$$

where σ_{η_i} is the standard deviation of the respective covariance matrix \mathbf{Q}_{η_i} . Eventually, two additional procedures are implemented in the navigation filter to face the errors of the IP algorithm:

- 1) When observations are not acquired due to an IP failure, the state vector and its error covariance matrix are simply propagated until the next step.
- 2) An innovation-based outlier detection method is applied to reject false positives [46]. In particular, when the absolute value of the innovation term $\|\mathbf{y}_k - \mathbf{h}(\mathbf{x}_{p_k})\|$ is greater than $k\sqrt{\mathbf{M}_{ii}}$ with $\mathbf{M} = \mathbf{H}_k \mathbf{P}_{p_k} \mathbf{H}_k^\top + \mathbf{R}_k$ and $k = 3$, the innovation term is set to zero, and the filter correction step is not performed. Indeed, it is preferred to keep an old but good prediction so as not to worsen the estimation.

V. Results

In this section, primarily, the performance of the IP is tested on a set of randomly generated scenarios. Specifically, a sensitivity analysis is carried on to analyze the IP behavior as the uncertainty on the probe position rises. Following this, the light-time delay analytic equation is verified, and the VBN filter is tested on an interplanetary trajectory. In particular, the impact of light time and light aberration on state estimation is assessed.

A. Image Processing Performance

To validate the IP algorithm performance before adopting it inside the VBN filter, four Monte Carlo (MC) campaigns are carried out to assess the robustness of the pipeline to the variation of the initial spacecraft pose uncertainty. The initial standard deviation of the probe position σ_r , which is used to compute the initial filter error covariance matrix (see Eq. 52), is set to 10^4 , 10^5 , 10^6 , and 10^7 km, respectively. In each campaign, the extraction of the beacon location is run for 1000 cases. In each scenario, the x and y components of the spacecraft position are sampled from uniform distribution $U(-3, 3)$ AU, while the z component is sampled from $U(-0.07, 0.07)$ AU. Note that a translation is then applied to center the spacecraft position in the origin of \mathcal{I} (i.e., the Solar System Barycenter). The z -component of the probe position is chosen in a narrower interval as the spacecraft is supposed to lie close to the ecliptic plane. Similarly, the orientation of the probe

is determined by sampling Euler angles from a uniform distribution. In particular the right ascension α is sampled from $U(0, 2\pi)$, the declination δ from $U(-0.6, 0.6)$, and the twist angle ϕ from $U(0, \pi)$. The declination δ is chosen in a narrower interval as planets are distributed close to the ecliptic plane. The images used to assess the IP performance are generated by adopting an extended and improved version of the sky-field rendering engine illustrated in Bella et al. [47]. In the image simulator, various effects coming from both external and internal sources are modeled and added to deep-space images, such as light effects and detector noises. For what concerns the planet identification step, σ_{q_v} is set equal to 20 arcsec as a result of a statistical analysis conducted on the error obtained in the attitude determination. The planet position uncertainty $\sigma_{r_{pi}}$ is assumed equal to zero because of the high accuracy with which the planets ephemeris are known. Note that, when other celestial objects are observed to navigate (e.g., asteroids [25] for deep space applications or debris [48] for Earth-based ones), their position and velocity uncertainties may be taken into account in the formulation by using Eq. 48.

to assess the algorithm behavior, the performance indexes adopted for their assessment are the angular error for the attitude determination and the beacon location error for the planet identification step. In detail, the attitude determination error is evaluated by the procedure adopted in Mortari et al. [33]. About the cross-boresight directions, the angular error is determined as

$$\sigma_{\text{Err}_{cb}} = \cos^{-1} \left({}^C \mathbf{z}^\top \mathbf{A}_e {}^C \mathbf{z} \right) \quad (53)$$

where $\mathbf{A}_e = \mathbf{A}_{\text{corr}} \mathbf{A}_{\text{true}}^\top$ is the error attitude matrix between the estimated and the real attitudes, and ${}^C \mathbf{z}$ is the boresight direction that corresponds to the body frame third axis. Conversely, the minimum and maximum values of the attitude determination error about the boresight direction are defined as

$$\sigma_{\text{Err}_{b\min}} = \cos^{-1} \left(\mathbf{w}^\top \mathbf{A}_e \mathbf{w} \right) \quad (54)$$

$$\sigma_{\text{Err}_{b\max}} = \cos^{-1} \left(\frac{\text{trace}(\mathbf{A}_e) - 1}{2} \right) \quad (55)$$

where

$$\mathbf{w} = \frac{{}^C \mathbf{z} \times ({}^C \mathbf{z} \times \mathbf{e})}{\|{}^C \mathbf{z} \times \mathbf{e}\|} \quad (56)$$

with \mathbf{e} the principal axis of the error attitude matrix \mathbf{A}_e .

For what concerns the planet centroid error, this latter is found by evaluating the difference between the position of the centroid identified as planet and the real planet position in the image.

The Probability Density Function (PDF) along with the 3σ ellipsoid of the best-fit Gaussian distribution for $\sigma_r = 10^4$ km, $\sigma_r = 10^5$ km, $\sigma_r = 10^6$ km, and $\sigma_r = 10^7$ km are shown in Figs. 2a, 2b, 2c, and 2d, respectively. Note that the planet location is detected with a sub-pixel 3σ accuracy for all the values of σ_r . In

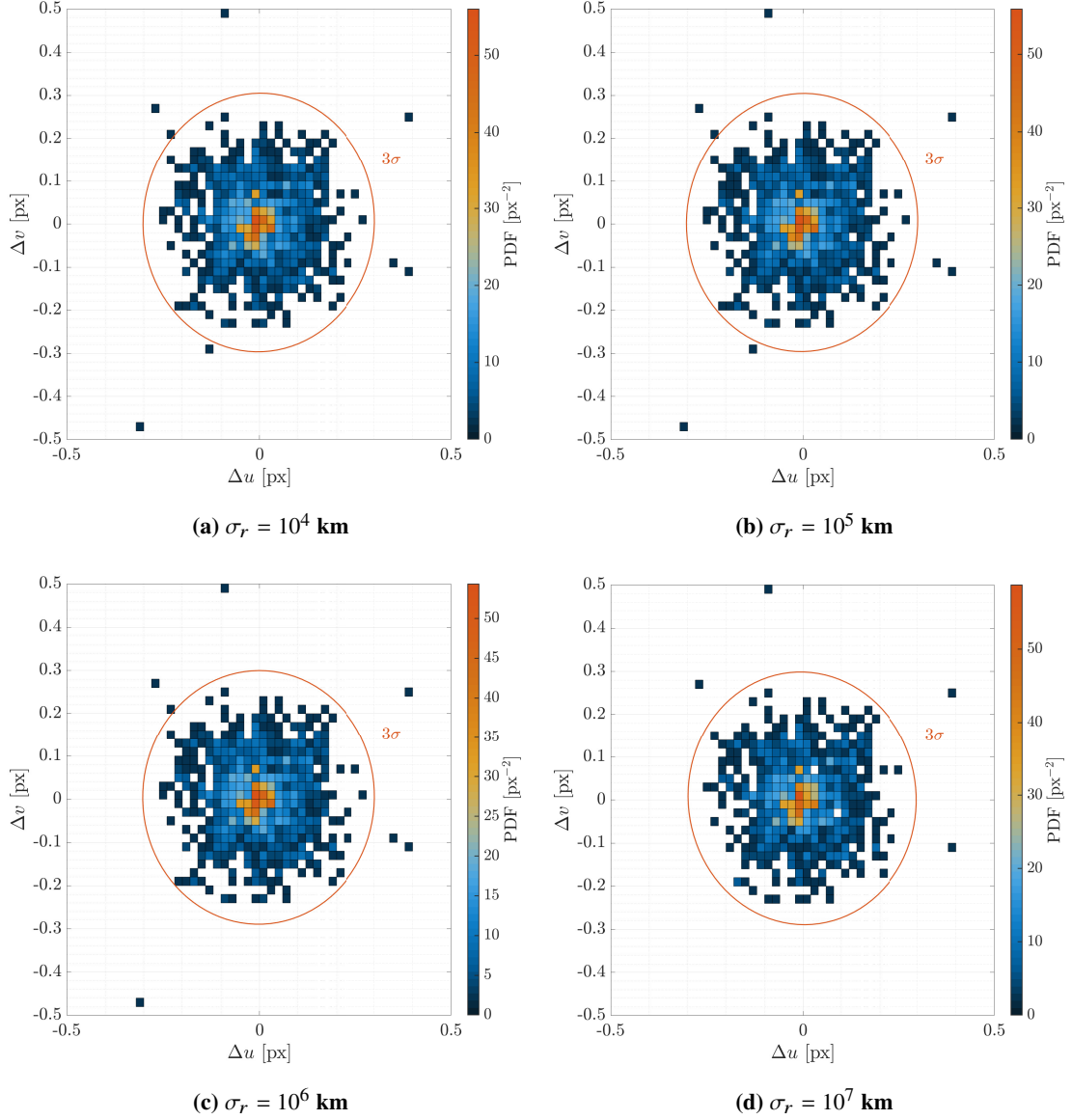


Fig. 2 Probability density function of the planet location errors with 3σ bounds

other terms, the error on the estimated planet location is not dependent on the probe position uncertainty but only on the attitude determination and centroids computation errors. The 3σ error ellipses in Fig. 2 are obtained from the mean and covariance values reported in Table 2.

The four covariance matrices are characterized by a similar determinant, which is proportional to the area of the ellipse, implying that the accuracy in the estimation of the planet location is not dependent on the uncertainty of the spacecraft position. This feature is one of the key aspects of the adopted pipeline. The results of the IP robustness and attitude determination error are shown in Table 3. The algorithm succeeds in determining the probe attitude in over 98% of the scenarios, independently of the probe position uncertainty. The slight variability observed in the no-attitude-determination cases is due to the random behavior of

Table 2 Mean and covariance of the planet location errors when the probe position uncertainty is known with an accuracy of 10^4 , 10^5 , 10^6 , and 10^7 km

σ_r [km]	\mathbf{P}_{err} [px ²]	$\boldsymbol{\mu}_{\text{err}}$ [px]	$\det(\mathbf{P})$ [px ⁴]
10^4	$\begin{bmatrix} 0.008 & 0.0001 \\ 0.0001 & 0.008 \end{bmatrix}$	$[-0.0007, 0.0045]$	$5.8715e - 05$
10^5	$\begin{bmatrix} 0.008 & 0.0001 \\ 0.0001 & 0.008 \end{bmatrix}$	$[-0.0012, 0.0046]$	$5.8778e - 05$
10^6	$\begin{bmatrix} 0.008 & 0 \\ 0 & 0.007 \end{bmatrix}$	$[-0.0011, 0.0052]$	$5.6399e - 05$
10^7	$\begin{bmatrix} 0.008 & -0.001 \\ -0.001 & 0.007 \end{bmatrix}$	$[-0.0011, 0.0049]$	$5.4618e - 05$

Table 3 Performances of the IP procedure in attitude determination and beacons identification

σ_r [km]	$\sigma_{\text{Err}_{\text{cb}}}/\sigma_{\text{Err}_{\text{bmax}}}$ [arcsec]	% Wrong Attitude Determination	% No Attitude Determination	% Correct Beacon Identification
10^4	2/13	0.5	0.8	98.75
10^5	2/13	0.5	0.6	98.75
10^6	2/13	0.5	0.9	98.24
10^7	2/14	0.5	1.1	81.28

the RANSAC algorithm. The attitude determination is considered wrong when $\sigma_{\text{Err}_{\text{bmax}}} > 1^\circ$. Conversely, the percentage of off-nominal scenarios during planet identification greatly depends on the probe position uncertainty. Indeed, when σ_r increases, the expected planet location is further from the real one, and its covariance ellipse gets larger, leading to a higher probability of planet misidentification. Moreover, the percentage of off-nominal scenarios in planet identification also depends strictly on the success of the attitude determination. Indeed, when attitude determination provides the wrong solution, planet identification fails consequentially. In Table 3, the fifth column represents the percentage of correct planet identification when the attitude determination converges to the right solution. The failure percentage of the beacon identification procedure, when the probe attitude is correctly determined, remains below 2% even with a probe position uncertainty of up to 10^5 km

In conclusion, the precision of the proposed method is independent of the probe position uncertainty, and it relies only on the center-finding performance (i.e., 0.1 pixels). Whereas, the robustness of the IP depends on the attitude determination performance and the probe position uncertainty. Indeed, the planet identification technique precision is not affected by the planet position determination, while its recall is affected by the increase in position uncertainty. It is worth noting that the recall degrades for a high value of the position

uncertainties (i.e., 0.01 AU). For completeness sake, Fig. 3 shows some scenarios found during the IP performance assessment where the procedure fails in planet identification. In particular, in Figs. 3a, 3b,

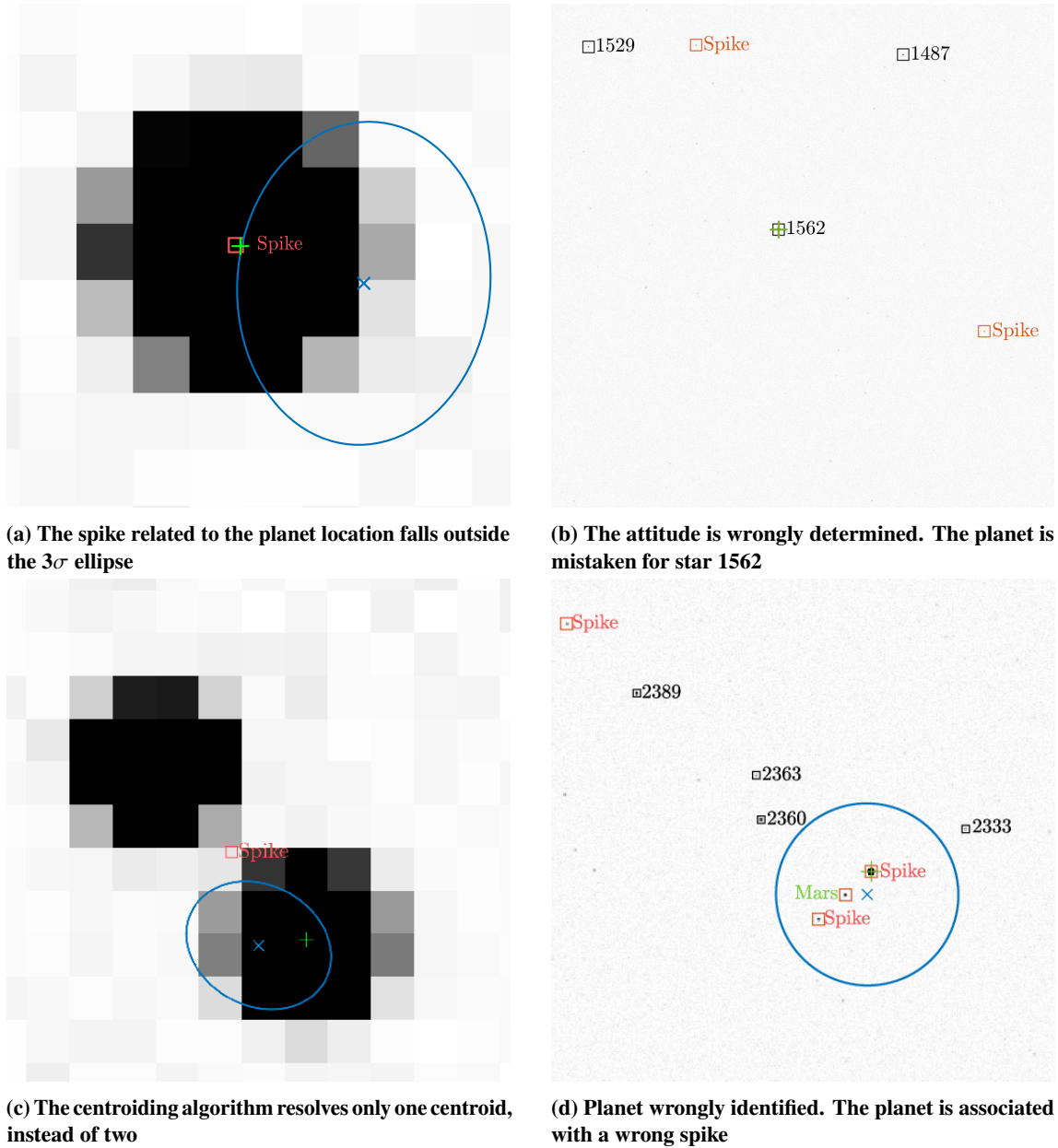


Fig. 3 Scenarios in which the IP pipeline fails in the planet identification. + represents the real planet location, x represents the expected planet location, and □ the found spikes, respectively

and 3c the planet is not found in the image, whereas in Fig. 3d the planet is wrongly determined. Regarding Figs. 3b and 3d, the off-nominal cases may be mitigated by applying the RANSAC procedure and the innovation-based outlier detection method, respectively.

B. Filter Results

1. Assessment of the analytical formulation of the light-time delay

This paragraph specifically investigates the computational time needed to implement the linear model in Eq. 37 and the resulting accuracy in the location of the planet affected by light time. Indeed, it is important to assess the performance of the novel proposed methodology with respect to state-of-the-art techniques in terms of accuracy and computational time. In the analyzed scenario, the light-time effect on the location of the first five planets with respect to an observer at the Solar-System Barycenter in the J200 reference frame is evaluated with the proposed approach and the iterative state-of-the-art solution [9, 19, 45]. The computed locations are then compared to the values found by SPICE[†] which is used as reference. The resulting accuracy in planet location and the computational time required to evaluate the light-time delay with the method proposed in this work are reported in the second and third columns of Table 4. It is worth noting that the computational time is not computed to assess the real performance of the algorithm in flight, but merely for the sake of comparison, given the MATLAB implementation. To fairly compare the performance of the proposed method with the state-of-the-art iterative Newton-Raphson’s approach, the number of iterations required to achieve the same order of accuracy in planet location is evaluated and reported in the sixth column of the table. Furthermore, the computational time needed to compute the light-time delay is outlined in the fifth column. Note that computational times have been computed by taking the average values over 1000 runs in both methods. By comparing the computational times, the proposed approach performs always better than the iterative one. Consequently, with equivalent accuracy, the proposed approximation proves to be significantly more computationally efficient than the iterative method. For the sake of completeness, the computational time needed to achieve a less stringent accuracy level of 0.04 pixels (i.e., one order below the accuracy of the IP) is also computed for the Mars case. The iterative method still takes 5 ms with 18 iterations, further supporting the preference for the proposed approach.

Table 4 Obtained accuracy in the estimation of the planet position affected by light time and required computational time to compute the time delay with the proposed method and the iterative approach

	Proposed method		Iterative approach		
	Accuracy [px]	CPU time [ms]	Accuracy [px]	CPU time [ms]	N iterations [-]
Mercury	2.32e-05	0.019	2.32e-05	3	18
Venus	8.15e-07	0.1	8.18e-07	48	23
Earth	4.37e-07	0.086	4.38e-07	53	24
Mars	1.28e-06	0.025	1.28e-06	6	21
Jupiter	5.42e-05	0.088	5.19e-05	37	22

[†]https://naif.jpl.nasa.gov/pub/naif/toolkit_docs/IDL/icy/cspice_spkezr.html, Last Visited on February 2024

2. Navigation Concept of Operations

In the study case, a CubeSat estimates its position and velocity by tracking visible planets over an interplanetary transfer. The spacecraft alternates observation windows, where an asynchronous tracking of the optimal pair of planets is performed, to only-propagation windows, where the filter only propagates the probe state as no external observations are acquired. The navigation Concept of Operations (CONOPS) is shown in Fig. 4. The probe tracks the first planet of the optimal pair, which is selected at the beginning of the navigation cycle, then performs a slew maneuver to point to the second planet, during which no observations are acquired, and it observes this later. Eventually, the estimation is propagated until the following observation window starts.

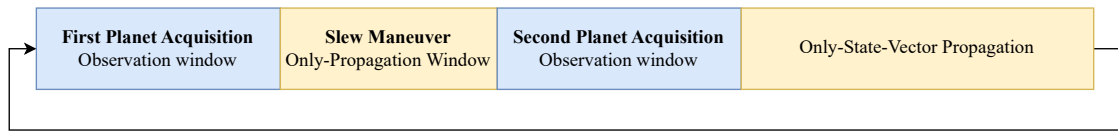


Fig. 4 Navigation concept of operations

At every time step of the planet observation, an image is generated using an improved version of the deep-space sky simulator in Bella et al. [47]. The simulator models the effects caused by the lights (i.e., light-time and light-aberration effects) on the centroids positions and by the impact of cosmic rays hitting the sensor frame. The sky simulator renders the image by taking into input the true probe pose and velocity. Since the attitude control system is not simulated in this work, the true probe orientation is computed by evaluating the desired pointing direction needed to acquire the planet at the center of the image and adding a random perturbation to it, which simulates the spacecraft jitter effect and the attitude knowledge error. Since the probe position is known with a given uncertainty (up to 10^5 km in this work), the beacon location will be not perfectly centered in the image, but still be contained in it, which is a sufficient condition to let the IP pipeline extract the planet observation.

3. Simulation Settings

The VBN filter proposed in this work is tested on an interplanetary high-fidelity ballistic trajectory between Earth–Mars [49]. The dynamics of the reference true trajectory include the SRP perturbations, the main attractor acceleration, third-body accelerations due to all the planets in the Solar System, and relativistic perturbations. Note that the dynamic model selected for the filter (Eq. 24) is a lower-fidelity one, implying that the unmodeled accelerations are captured by the GM processes. Fig. 5 shows the analyzed leg of the nominal probe trajectory. Note that this is an improvement with respect to Andreis et al. [9] where simpler dynamics models are used in the filter and in the truth simulation.

Starting from t_0 , the estimation procedure begins. Each planet is tracked for an hour with a frequency

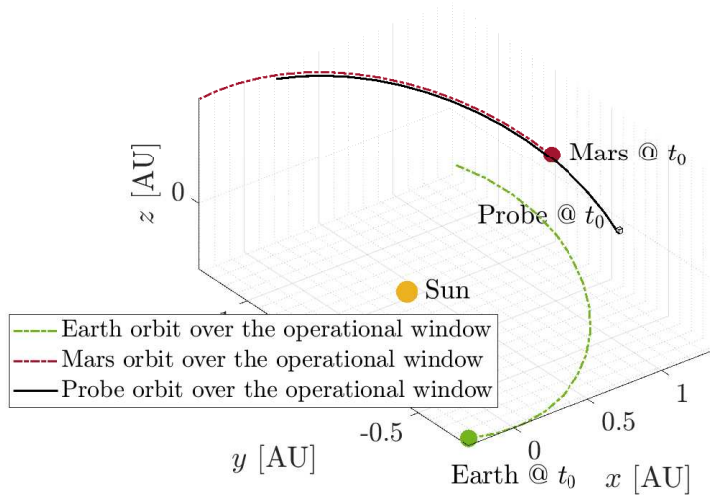


Fig. 5 Ballistic interplanetary reference trajectory

of 0.01 Hz, the slew maneuver lasts 30 minutes, and the window in which the state is only propagated is ten days. Therefore, only two hours every ten days are reserved for correcting the state estimate. Over the interplanetary trajectory, 10 navigation legs of 10 days 2 hours, and 30 minutes each are repeated.

For image generation, the onboard camera is assumed to have the characteristics reported in Table 5, where F is the f-number, Q_e is the quantum efficiency, T_{lens} is the lens transmission, σ_d is the defocus level, and n_{CR} is the number of single pixels that are turned on for simulating the presence of hitting cosmic rays. Figs. 6a and 6b are two of the rendered deep-space sky images adopted in the filtering procedure. For what

Table 5 Onboard Camera Characteristics

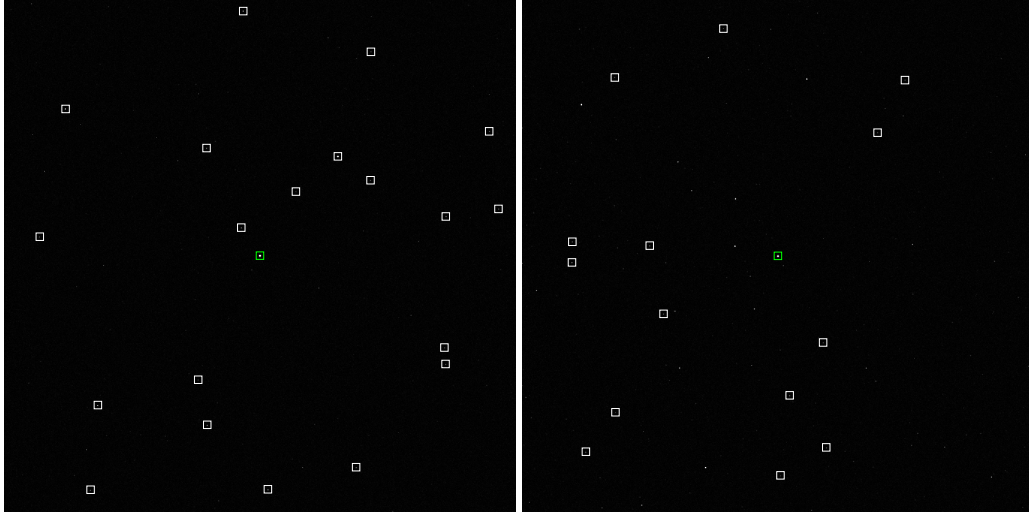
FoV [deg]	F [-]	T [ms]	Image size [px]	f [mm]	$Q_e \times T_{\text{lens}}$	σ_d [px]	n_{CR}	SEA
20	2.2	400	1024 × 1024	40	0.49	0.5	3	20

concerns the IP, the parameters adopted in the thresholding step and the RANSAC are detailed in Table 6. In detail, k_{thr} is the tuning parameter of the Niblack's method, n_R is the total number of samples considered, m_R is the number of centroids for each sample, and t_R is the threshold value considered for data fitting. More details about the RANSAC procedure can be found in Andreis et al. [24].

Table 6 Parameters of the RANSAC and thresholding procedures

k_{thr} [-]	n_R [-]	m_R [-]	t_R [arcsec]
10	30	3	100

The initial standard deviations of the state adopted in Eq. 52 are reported in Table 7.



(a) Image taken during Earth observation in LIS mode (b) Image taken during Mars observation in LIS mode

Fig. 6 Generated sky-field images. The planet is outlined with a green marker and identified stars with a white marker

Table 7 Accuracy of the state components at t_0

σ_r [km]	σ_v [km/s]	$\sigma_{\eta_{SRP}}$ [km/s ²]	σ_{η_R} [km/s ²]
10^4	10^{-1}	10^{-11}	10^{-11}

Note that the values are selected following a conservative approach, taking into account that in deep space the initial position and velocity are usually known with an accuracy better than 10^4 km and 0.1 km/s, respectively. However, even if the performance of the IP procedure degrades by increasing the probe position uncertainty, this has been tested to work up to $\sigma_r = 10^6$ km with a success rate higher than 90% in planet identification. Then, the performance of the IP worsens to 70% when $\sigma_r = 10^7$ km (see Sec. V.A). For what concerns the OD, in Andreis et al. [9] the algorithm is tested to work up to $\sigma_r = 10^7$ km. Over this value, the OD algorithm is not able to select the optimal targets.

The SRP has been modeled with a steady-state standard deviation of 10% of the nominal value as in Yárnoz et al. [50], which corresponds approximately to 10^{-11} km/s⁻² at the beginning of the trajectory and with 10 days of correlation time. Eventually, residual accelerations, which include also errors due to attitude control maneuvers, have been modeled with a steady-state standard deviation of 10^{-11} km/s⁻² and a correlation time of 1 day [50]. Moreover, the standard deviation of the measurement error is set to $\sigma_{str} = 0.1$ px, considering the results of the Monte Carlo runs in the extraction of the planet centroid reported in Sec. V.A. Eventually, only planets whose apparent magnitude is lower than 7 and whose SEA is greater than 20° are assumed to be visible by the camera. Therefore, they are the only ones considered available for the optimal beacon selection

process. It is worth noting that all the planets have been considered in the image simulation, implying that the ones not fulfilling the above conditions could be identified as outliers and degrade the IP performance.

4. Filter Performance

To evaluate the filter performance, a Monte Carlo simulation of 100 samples is performed. The lower number of simulations is due to the need to simulate long propagation arcs and the large number of images for every Monte Carlo sample. Figures 7 and 8 show the position and velocity error profiles and 3σ covariance bounds in the J2000 ecliptic reference frame on the studied trajectory leg. The sample error profile is displayed with blue solid lines, whereas the orange solid lines and the dashed ones define the 3σ covariance bounds of the samples and the filter, respectively.

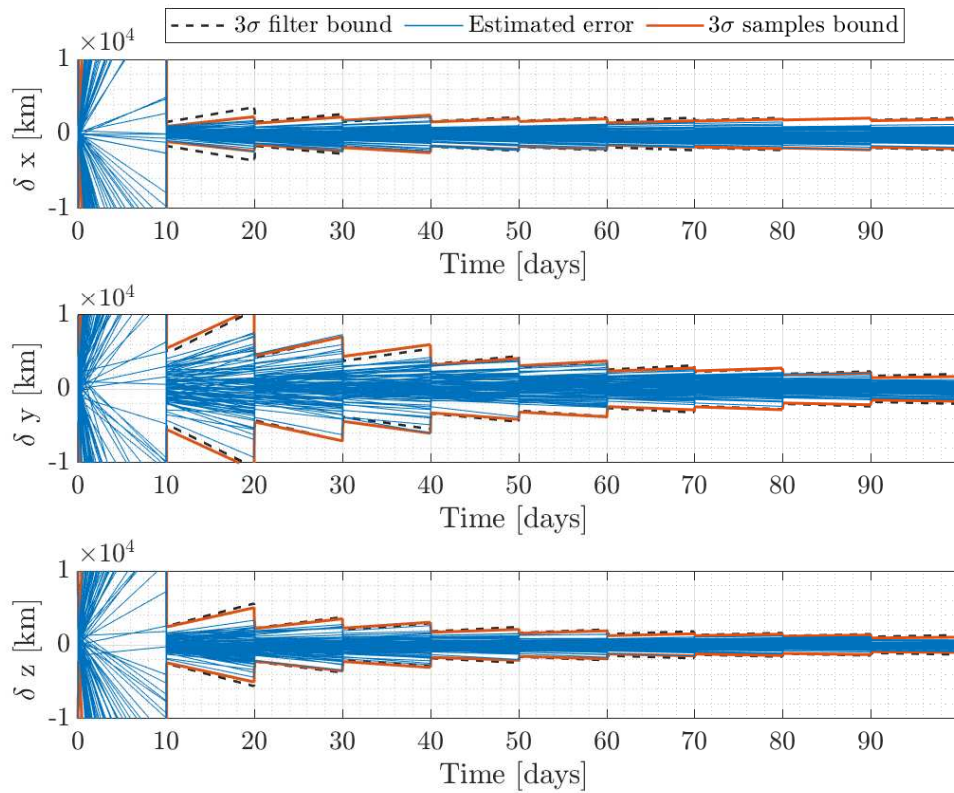


Fig. 7 Estimated errors for each position component with related 3σ bounds

At the end of the trajectory leg, the filter estimates the spacecraft position and velocity with a 3σ accuracy of 3200 km and 0.8 m/s, respectively. The 3σ sample and filter covariance profiles are mostly overlapped, which suggests that the filter and its covariance matrices, in particular \mathbf{R} , are well tuned. This underlines that the planet centroids are extracted with a 3σ accuracy lower than 0.3 px as found in the Monte Carlo campaigns conducted in Sec. V.A. For the 100-sample Monte Carlo run, the total number of outliers detected by the algorithm is 4. Considering that 740 images are processed for each sample, this means that in 0.005%

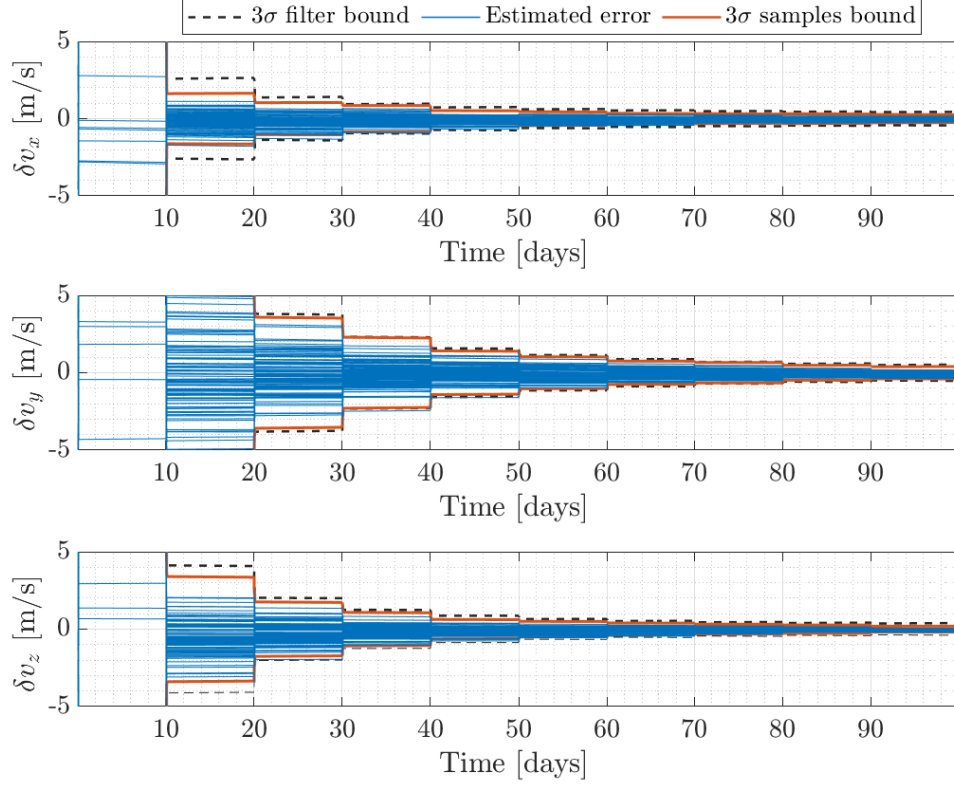


Fig. 8 Estimated errors for each velocity component with related 3σ bounds

of the cases, an outlier is found. The planets observed during the interplanetary transfer are Earth, Mars, and Venus. Their object-to-pixel ratio is checked to be below 1 over the entire tracking period to respect the assumption of navigation with unresolved planets. The performance of the filter detailed above where both light effects acting on the position of the planets are corrected is labeled MC1 in the following discussion and it is compared with the other 4 cases, which are:

MC2: Only a correction of the light-time effect acting on the position of the planets. The measurement model is defined by Eqs. 49 and 50;

MC3: Only a correction of the light-aberration effect acting on the position of the planets. Therefore, $\Delta t = 0$ and $\delta\Delta t = 0$ in Eqs. 37 and 47;

MC4: No correction of the light effects acting on the position of the planets. The measurement model is defined by Eqs. 49 and 50 with $\Delta t = 0$ and $\delta\Delta t = 0$ in Eqs.37 and 47;

MC5: A correction of the light-time effect acting on the position of the planets. Hence, the measurement model is defined by Eqs. 49 and 50. Furthermore, the stellar light aberration is not corrected in the IP.

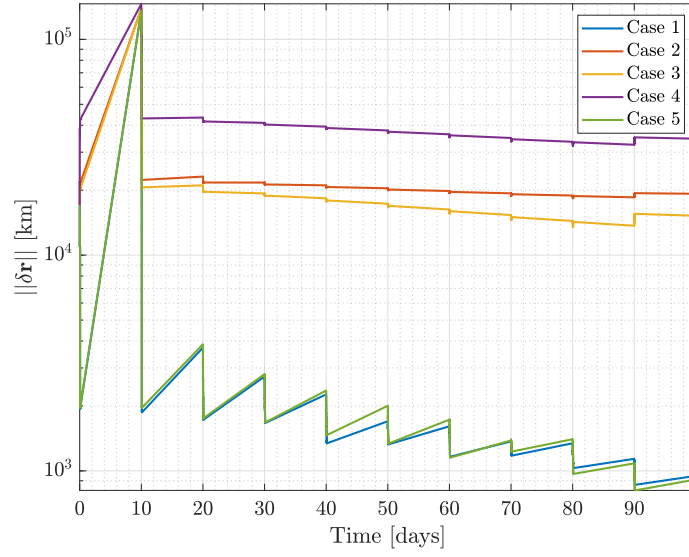
Note that in the first four Monte Carlo simulations (i.e., MC1, MC2, MC3, and MC4), the stellar aberration correction is always implemented in the IP (see Sec. III.B) despite what is implemented in the measurement

model. This assumption was performed to generalize the analysis to the case in which an attitude estimation already compensated for light aberration is provided to the filter either by the attitude determination and control system or directly from a star tracker. Moreover, an uncorrected attitude would induce a constant bias in the filter, leading to an unfair comparison among the different implementations. Therefore, the analysis is focused on the potential implications if the planets locations remain uncorrected for light effects. Conversely, the last MC study is relevant when the same optical camera exploited for navigation serves for attitude determination. In this case, the option to not compensate for stellar aberration exists, potentially yielding an aberrated attitude value. Hence, this scenario explores situations where neither stellar nor planetary aberrations are corrected.

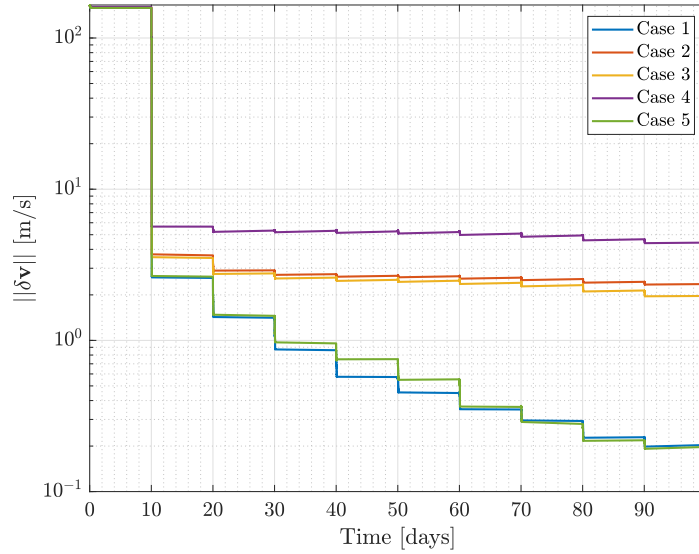
The root-mean-square error (RMSE) is chosen as the performance index to measure the estimation accuracy of the different models for the selected dataset as it captures effects due to mean (e.g., biases) and covariance of the estimated solution. The latter comprises 100 initial state vectors and 740 images for simulation representing the scenarios observed during the interplanetary transfer. The filter and camera settings are unchanged with respect to MC1 for the sake of comparison.

Fig. 9 shows the results of the analysis. The most significant deviation from the nominal value, represented by MC1 and whose components are shown in Figs. 7 and 8, occurs when both light effects corrections are not taken into account in the filter (MC4). Between the two effects, the greatest deviation from the nominal value is obtained when the light-aberration effect remains uncompensated (MC2), compared to the scenario where the light-time effect is corrected (MC3). When the light aberration correction is not applied on both the stars and planets centroids, the probe state estimation is affected by a negligible deviation (MC5). This occurs since, being the attitude adopted in the measurement model equation determined directly from the image, the light aberration affects similarly the measurement model and the external observation. Therefore, it is evident that when the same optical sensor is adopted for attitude determination and navigation, the light-aberration correction may not be necessary, saving computational time.

Eventually, validation of the VBN filter performance can be achieved by comparing results with those obtained from a concurrent in-flight demonstration of celestial triangulation with distant planets [51]. This validation repeats the simulation on the ballistic Martian corridor by setting position and velocity uncertainties to values matching those utilized in the in-flight testing (i.e., $\sigma_r = 10^5$ km and $\sigma_v = 1$ km/s). During the demonstration, observations of Jupiter, Mars, and Saturn were made 8 times, once, and 7 times respectively, with measurement errors set at 0.5 px, 0.75 px, and 0.25 px. To accurately model the measurement error covariance matrix in the implemented filter, unit measurement uncertainty is set to $\sigma_{str} = 0.2 = 0.4 * 36.6/67$, considering an weighted average value for the measurement error in pixels (i.e., 0.4 pixel) multiplied by the camera iFoV specified in Krause et al. [51] (i.e., 36.6 arcsec) and divided by the camera iFoV employed in the current simulation (i.e., 67 arcsec). This is done to compare measurements with the same angular error



(a) Position RMSE



(b) Velocity RMSE

Fig. 9 Comparison of the performance of the filter under various light effects

despite the camera carried on board and eventual calibration residual errors. Additionally, the implemented filter assumes to acquire only 16 observations throughout the trajectory to match the number of images adopted in the in-flight testing. At the end of the trajectory, the filter estimates position and velocity with a 3σ accuracy of 12000 km and 2.15 m/s respectively. The order of magnitude of the obtained residuals is consistent with the one found in Krause et al. [51] (i.e., 60000 km and 5 m/s).

VI. Conclusion

This paper develops an autonomous vision-based navigation algorithm for interplanetary transfer with an application for CubeSats missions. An extended Kalman filter adopting the planet location as external observation is chosen by considering the limited processing capabilities of a standard miniaturized processor. Moreover, the measurements exploited for the estimation correction are directly extracted from images generated with a deep-space rendering engine. This procedure allows for obtaining a more faithful value of the measurement error and its influence on the filter solution. At the end of the Earth–Mars trajectory, the filter estimates the spacecraft position and velocity with an accuracy of 2000 km and 0.5 m/s, respectively. Future analysis should examine the performance of the filter over low-thrust trajectories, which are desirable in CubeSats applications. Moreover, this work determines the probe attitude from deep-space images with state-of-the-art star identification and attitude determination algorithms. Integrating the attitude filter in the proposed vision-based navigation algorithm is object of future investigation. Eventually, to validate the vision-based navigation applicability, it will be tested through hardware-in-the-loop simulations. Preliminary results have already been obtained through, first, the validation of the orbit determination algorithm with processor-in-the-loop simulations [9] and, second, with the validation of the image processing pipeline with the optical facility in the loop [52–55]. More details about the validation and verification procedure carried on to increase the TRL of the navigation algorithm within the EXTREMA project are reported in Di Domenico et al. [56] and Di Domenico et al. [57].

Acknowledgments

This research is part of EXTREMA, a project that has received funding from the European Research Council (ERC) under the European Union’s Horizon 2020 research and innovation programme (Grant Agreement No. 864697).

Appendix

A. Useful matrices to compute derivatives of the measurement model

$$\begin{aligned}
 \mathbf{R}_{sc} = & \left(\mathbf{I}_{3 \times 3} + 2 \boldsymbol{\beta}_{sc} \mathbf{l}_{pl/sc}^\top - \mathbf{l}_{pl/sc}^\top \boldsymbol{\beta}_{sc} \mathbf{I}_{3 \times 3} - \mathbf{l}_{pl/sc} \boldsymbol{\beta}_{sc}^\top \right) \left(\frac{\mathbf{I}_{3 \times 3}}{\left\| \left(\mathbf{r}_{pl}(t - \Delta t) - \mathbf{r}(t) \right)^\top \left(\mathbf{r}_{pl}(t - \Delta t) - \mathbf{r}(t) \right) \right\|} \right) + \\
 & - \frac{\left(\mathbf{r}_{pl}(t - \Delta t) - \mathbf{r}(t) \right) \left(\mathbf{r}_{pl}(t - \Delta t) - \mathbf{r}(t) \right)^\top}{\left\| \left(\mathbf{r}_{pl}(t - \Delta t) - \mathbf{r}(t) \right)^\top \left(\mathbf{r}_{pl}(t - \Delta t) - \mathbf{r}(t) \right) \right\|^3} \right) \left(\frac{\mathbf{v}_{pl}}{c^2 - \mathbf{v}_{pl}(t)^\top \mathbf{v}_{pl}(t)} \right. \\
 & \left. \left(\frac{\left(c^2 - \mathbf{v}_{pl}(t)^\top \mathbf{v}_{pl}(t) \right) \mathbf{r}_{pl/sc}(t)^\top + \mathbf{r}_{pl/sc}(t)^\top \mathbf{v}_{pl}(t) \mathbf{v}_{pl}(t)^\top}{\sqrt{\mathbf{r}_{pl/sc}(t)^\top \mathbf{r}_{pl/sc}(t) \left(c^2 - \mathbf{v}_{pl}(t)^\top \mathbf{v}_{pl}(t) \right) + \left(\mathbf{r}_{pl/sc}(t)^\top \mathbf{v}_{pl}(t) \right)^2}} - \mathbf{v}_{pl}^\top(t)} \right) - \mathbf{I}_{3 \times 3} \right) \quad (57)
 \end{aligned}$$

$$\mathbf{V}_{sc} = \frac{1}{c} \left(\mathbf{l}_{pl/sc}^\top \mathbf{I}_{pl/sc} \mathbf{I}_{3 \times 3} - \mathbf{l}_{pl/sc} \mathbf{I}_{pl/sc}^\top \right) \quad (58)$$

$$\mathbf{Q}_{att} = 2 \left[\mathbf{l}_{pl/sc}^{aberr} \right]^\wedge \quad (59)$$

$$\begin{aligned}
 \mathbf{R}_{pl} = & \left(\mathbf{I}_{3 \times 3} + 2 \boldsymbol{\beta}_{sc} \mathbf{l}_{pl/sc}^\top - \mathbf{l}_{pl/sc}^\top \boldsymbol{\beta}_{sc} \mathbf{I}_{3 \times 3} - \mathbf{l}_{pl/sc} \boldsymbol{\beta}_{sc}^\top \right) \left(\frac{\mathbf{I}_{3 \times 3}}{\left\| \left(\mathbf{r}_{pl}(t - \Delta t) - \mathbf{r}(t) \right)^\top \left(\mathbf{r}_{pl}(t - \Delta t) - \mathbf{r}(t) \right) \right\|} \right) + \\
 & - \frac{\left(\mathbf{r}_{pl}(t - \Delta t) - \mathbf{r}(t) \right) \left(\mathbf{r}_{pl}(t - \Delta t) - \mathbf{r}(t) \right)^\top}{\left\| \left(\mathbf{r}_{pl}(t - \Delta t) - \mathbf{r}(t) \right)^\top \left(\mathbf{r}_{pl}(t - \Delta t) - \mathbf{r}(t) \right) \right\|^3} \right) \left(\mathbf{I}_{3 \times 3} + \right. \\
 & \left. - \frac{\mathbf{v}_{pl}}{c^2 - \mathbf{v}_{pl}(t)^\top \mathbf{v}_{pl}(t)} \left(\frac{\left(c^2 - \mathbf{v}_{pl}(t)^\top \mathbf{v}_{pl}(t) \right) \mathbf{r}_{pl/sc}(t)^\top + \mathbf{r}_{pl/sc}(t)^\top \mathbf{v}_{pl}(t) \mathbf{v}_{pl}(t)^\top}{\sqrt{\mathbf{r}_{pl/sc}(t)^\top \mathbf{r}_{pl/sc}(t) \left(c^2 - \mathbf{v}_{pl}(t)^\top \mathbf{v}_{pl}(t) \right) + \left(\mathbf{r}_{pl/sc}(t)^\top \mathbf{v}_{pl}(t) \right)^2}} - \mathbf{v}_{pl}^\top(t)} \right) \right) \quad (60)
 \end{aligned}$$

$$\begin{aligned}
 \mathbf{V}_{pl} = & - \left(\mathbf{I}_{3 \times 3} + 2 \boldsymbol{\beta}_{sc} \mathbf{l}_{pl/sc}^\top - \mathbf{l}_{pl/sc}^\top \boldsymbol{\beta}_{sc} \mathbf{I}_{3 \times 3} - \mathbf{l}_{pl/sc} \boldsymbol{\beta}_{sc}^\top \right) \left(\frac{\mathbf{I}_{3 \times 3}}{\left\| \left(\mathbf{r}_{pl}(t - \Delta t) - \mathbf{r}(t) \right)^\top \left(\mathbf{r}_{pl}(t - \Delta t) - \mathbf{r}(t) \right) \right\|} \right) + \\
 & - \frac{\left(\mathbf{r}_{pl}(t - \Delta t) - \mathbf{r}(t) \right) \left(\mathbf{r}_{pl}(t - \Delta t) - \mathbf{r}(t) \right)^\top}{\left\| \left(\mathbf{r}_{pl}(t - \Delta t) - \mathbf{r}(t) \right)^\top \left(\mathbf{r}_{pl}(t - \Delta t) - \mathbf{r}(t) \right) \right\|^3} \right) \left(\Delta t \mathbf{I}_{3 \times 3} + \right. \\
 & + \frac{\mathbf{v}_{pl}}{c^2 - \mathbf{v}_{pl}(t)^\top \mathbf{v}_{pl}(t)} \left(\frac{\mathbf{r}_{pl/sc}(t)^\top \mathbf{v}_{pl}(t) \mathbf{r}_{pl/sc}(t)^\top - \mathbf{r}_{pl/sc}(t)^\top \mathbf{r}_{pl/sc}(t) \mathbf{v}_{pl}(t)^\top}{\sqrt{\mathbf{r}_{pl/sc}(t)^\top \mathbf{r}_{pl/sc}(t) \left(c^2 - \mathbf{v}_{pl}(t)^\top \mathbf{v}_{pl}(t) \right) + \left(\mathbf{r}_{pl/sc}(t)^\top \mathbf{v}_{pl}(t) \right)^2}} \right. \\
 & \left. \left. + \frac{2 \mathbf{v}_{pl}(t)^\top}{c^2 - \mathbf{v}_{pl}(t)^\top \mathbf{v}_{pl}(t)} - \mathbf{r}_{pl/sc}(t)^\top \right) \right) \quad (61)
 \end{aligned}$$

References

- [1] Wang, Y., Zheng, W., Sun, S., and Li, L., “X-ray Pulsar-Based Navigation Using Time-Differenced Measurement,” *Aerospace Science and Technology*, Vol. 36, July 2014, pp. 27–35. <https://doi.org/https://doi.org/10.1016/j.ast.2014.03.007>.
- [2] Malgarini, A., Franzese, V., and Topputo, F., “Application of Pulsar-Based Navigation for Deep-Space CubeSats,” *Aerospace*, Vol. 10, No. 8, 2023, p. 695. <https://doi.org/https://doi.org/10.3390/aerospace10080695>.
- [3] Thornton, C. L., and Border, J. S., *Future Directions in Radiometric Tracking*, 1st ed., John Wiley & Sons, Ltd, New Jersey, United States, 2003, Chap. 5, pp. 63–75. <https://doi.org/https://doi.org/10.1002/0471728454.ch5>.
- [4] Henry, S., and Christian, J. A., “Absolute Triangulation Algorithms for Space Exploration,” *Journal of Guidance, Control, and Dynamics*, Vol. 46, No. 1, 2023, pp. 21–46. <https://doi.org/https://doi.org/10.2514/1.G006989>.
- [5] Maass, B., Woicke, S., Oliveira, W. M., Razgus, B., and Krüger, H., “Crater Navigation System for Autonomous Precision Landing on the Moon,” *Journal of Guidance, Control, and Dynamics*, Vol. 43, No. 8, 2020, pp. 1414–1431. <https://doi.org/https://doi.org/10.2514/1.G004850>.
- [6] Turan, E., Speretta, S., and Gill, E., “Autonomous Navigation for Deep-Space Small Satellites: Scientific and Technological Advances,” *Acta Astronautica*, Vol. 193, April 2022, pp. 56–74. <https://doi.org/https://doi.org/10.1016/j.actaastro.2021.12.030>.
- [7] Bhaskaran, S., Riedel, J., Synnott, S., and Wang, T., “The Deep Space 1 Autonomous Navigation System-A Post-Flight Analysis,” *Astrodynamics Specialist Conference*, AIAA, Denver, CO, USA, 2000. <https://doi.org/https://doi.org/10.2514/6.2000-3935>.
- [8] Franzese, V., Topputo, F., Ankersen, F., and Walker, R., “Deep-Space Optical Navigation for M-ARGO Mission,” *The Journal of the Astronautical Sciences*, Vol. 68, No. 4, 2021, pp. 1034–1055. <https://doi.org/https://doi.org/10.1007/s40295-021-00286-9>.
- [9] Andreis, E., Franzese, V., and Topputo, F., “Onboard Orbit Determination for Deep-Space CubeSats,” *Journal of Guidance, Control, and Dynamics*, Vol. 45, No. 8, 2022, pp. 1466–1480. <https://doi.org/10.2514/1.G006294>.
- [10] Merisio, G., and Topputo, F., “Present-Day Model of Lunar Meteoroids and Their Impact Flashes for LUMIO Mission,” *Icarus*, Vol. 389, January 2023, p. 115180. <https://doi.org/https://doi.org/10.1016/j.icarus.2022.115180>.
- [11] Panicucci, P., Lebreton, J., Brochard, R., Zenou, E., and Delpech, M., “Shadow-Robust Silhouette Reconstruction for Small-Body Applications,” *Journal of Spacecraft and Rockets*, Vol. 60, No. 3, 2023, pp. 812–828. <https://doi.org/https://doi.org/10.2514/1.A35444>.
- [12] Panicucci, P., Lebreton, J., Brochard, R., Zenou, E., and Delpech, M., “Vision-based estimation of small body rotational state,” *Acta Astronautica*, Vol. 213, December 2023, pp. 177–196. <https://doi.org/https://doi.org/10.1016/j.actaastro.2023.08.046>.

- [13] Pugliatti, M., Franzese, V., and Topputo, F., “Data-Driven Image Processing for Onboard Optical Navigation Around a Binary Asteroid,” Journal of Spacecraft and Rockets, Vol. 59, No. 3, 2022, pp. 943–959. <https://doi.org/https://doi.org/10.2514/1.A35213>.
- [14] McCarthy, L. K., Adam, C. D., Leonard, J. M., Antresian, P. G., Nelson, D., Sahr, E., Pelgrift, J., Lessac-Chenen, E. J., Geeraert, J., and Lauretta, D., “OSIRIS-REx Landmark Optical Navigation Performance During Orbital and Close Proximity Operations at Asteroid Bennu,” AIAA SCITECH 2022 Forum, AIAA, San Diego, CA & Virtual, January 2022. <https://doi.org/10.2514/6.2022-2520>.
- [15] Leroy, B., Medioni, G., Johnson, E., and Matthies, L., “Crater detection for autonomous landing on asteroids,” Image and Vision Computing, Vol. 19, No. 11, 2001, pp. 787–792. [https://doi.org/https://doi.org/10.1016/S0262-8856\(00\)00111-6](https://doi.org/https://doi.org/10.1016/S0262-8856(00)00111-6).
- [16] Bhaskaran, S., “Autonomous Navigation for Deep Space Missions,” SpaceOps 2012, AIAA, Stockholm, Sweden, June 2012. <https://doi.org/https://doi.org/10.2514/6.2012-1267135>.
- [17] Norman, C., Miller, C., Olds, R., Mario, C., Palmer, E., Barnouin, O., Daly, M., Weirich, J., Seabrook, J., Bennett, C., et al., “Autonomous Navigation Performance Using Natural Feature Tracking during the OSIRIS-REx Touch-and-Go Sample Collection Event,” The Planetary Science Journal, Vol. 3, No. 5, 2022, p. 101. <https://doi.org/10.3847/PSJ/ac5183>.
- [18] Topputo, F., Wang, Y., Giordano, C., Franzese, V., Goldberg, H., Perez-Lissi, F., and Walker, R., “Envelop of Reachable Asteroids by M-ARGO CubeSat,” Advances in Space Research, Vol. 67, No. 12, 2021, pp. 4193–4221. <https://doi.org/https://doi.org/10.1016/j.asr.2021.02.031>.
- [19] Karimi, R. R., and Mortari, D., “Interplanetary Autonomous Navigation Using Visible Planets,” Journal of Guidance, Control, and Dynamics, Vol. 38, No. 6, 2015, pp. 1151–1156. <https://doi.org/https://doi.org/10.2514/1.G000575>.
- [20] Casini, S., Cervone, A., Monna, B., and Gill, E., “On line-of-sight navigation for deep-space applications: A performance analysis,” Advances in Space Research, Vol. 72, No. 7, 2023, pp. 2994–3008. <https://doi.org/https://doi.org/10.1016/j.asr.2022.12.017>.
- [21] Stastny, N. B., and Geller, D. K., “Autonomous Optical Navigation at Jupiter: a Linear Covariance Analysis,” Journal of Spacecraft and Rockets, Vol. 45, No. 2, 2008, pp. 290–298. <https://doi.org/https://doi.org/10.2514/1.28451>.
- [22] Bhaskaran, S., “Autonomous Optical-Only Navigation for Deep Space Missions,” ASCEND 2020, AIAA, Virtual Event, November 16-18, 2020. <https://doi.org/https://doi.org/10.2514/6.2020-4139>.
- [23] Vaughan, R., Riedel, J., Davis, R., OWEN, W., JR, and Synnott, S., “Optical Navigation for the Galileo Gaspra Encounter,” Astrodynamics Conference, AIAA, Hilton Head Island, SC, U.S.A., August 1992. <https://doi.org/10.2514/6.1992-4522>.

- [24] Andreis, E., Panicucci, P., Franzese, V., and Topputo, F., "A Robust Image Processing Pipeline for Planets Line-Of-Sight Extraction for Deep-Space Autonomous Cubesats Navigation," 44th AAS Guidance, Navigation and Control Conference, AAS, Breckenridge, CO, USA, February 2022.
- [25] Broschart, S. B., Bradley, N., and Bhaskaran, S., "Kinematic Approximation of Position Accuracy Achieved Using Optical Observations of Distant Asteroids," Journal of Spacecraft and Rockets, Vol. 56, No. 5, 2019, pp. 1383–1392. <https://doi.org/10.2514/1.A34354>.
- [26] Franzese, V., and Topputo, F., "Celestial Bodies Far-Range Detection with Deep-Space CubeSats," Sensors, Vol. 23, No. 9, 2023, p. 4544. <https://doi.org/https://doi.org/10.3390/s23094544>.
- [27] Franzese, V., and Topputo, F., "Optimal Beacons Selection for Deep-Space Optical Navigation," The Journal of the Astronautical Sciences, Vol. 67, No. 4, 2020, pp. 1775–1792. <https://doi.org/https://doi.org/10.1007/s40295-020-00242-z>.
- [28] Lai, Y., Liu, J., Ding, Y., Gu, D., and Yi, D., "Attitude aberration correction for space technology experiment and climate exploration (STECE) satellite star tracker," Proceedings of the Institution of Mechanical Engineers, Part G: Journal of Aerospace Engineering, Vol. 229, No. 6, 2015, pp. 1142–1153. <https://doi.org/10.1177/0954410014547440>.
- [29] Jørgensen, J. L., Denver, T., Betto, M., and den Braembussche, P. V., "The PROBA satellite star tracker performance," Acta Astronautica, Vol. 56, No. 1, 2005, pp. 153–159. <https://doi.org/https://doi.org/10.1016/j.actaastro.2004.09.011>.
- [30] Kazemi, L., Enright, J., and Dzamba, T., "Improving Star Tracker Centroiding Performance in Dynamic Imaging Conditions," 2015 IEEE Aerospace Conference, IEEE, Big Sky, MT, USA, 2015, pp. 1–8. <https://doi.org/10.1109/AERO.2015.7119226>.
- [31] Wan, X., Wang, G., Wei, X., Li, J., and Zhang, G., "Star Centroiding Based on Dast Gaussian Fitting for Star Sensors," Sensors, Vol. 18, No. 9, 2018, p. 2836. <https://doi.org/10.3390/s18092836>.
- [32] Vyas, A., Roopashree, M., Prasad, B., and Vyas, A., "Performance of Centroiding Algorithms at Low Light Level Conditions in Adaptive Optics," 2009 International Conference on Advances in Recent Technologies in Communication and Computing, IEEE, Kottayam, India, October 2009, pp. 366–369. <https://doi.org/10.1109/ARCom.2009.30>.
- [33] Mortari, D., Samaan, M. A., Bruccoleri, C., and Junkins, J. L., "The Pyramid Star Identification Technique," Navigation, Vol. 51, No. 3, 2004, pp. 171–183. <https://doi.org/https://doi.org/10.1002/j.2161-4296.2004.tb00349.x>.
- [34] Bentley, J. L., and Sedgewick, R., "Fast algorithms for sorting and searching strings," Proceedings of the Eighth Annual ACM-SIAM Symposium on Discrete Algorithms, Society for Industrial and Applied Mathematics, USA, 1997, p. 360–369.

- [35] Mortari, D., and Neta, B., “K-vector range searching techniques,” Adv. Astronaut. Sci., Vol. 105, No. 1, 2000, pp. 449–464. URL <https://hdl.handle.net/10945/41061>.
- [36] Rijlaarsdam, D., Yous, H., Byrne, J., Oddenino, D., Furano, G., and Moloney, D., “A Survey of Lost-in-Space Star Identification Algorithms Since 2009,” Sensors, Vol. 20, No. 9, 2020, p. 2579. <https://doi.org/10.3390/s20092579>.
- [37] Markley, F. L., and Crassidis, J. L., Fundamentals of Spacecraft Attitude Determination and Control, 1st ed., Springer, New York, 2014, Chap. 5, pp. 183–235. <https://doi.org/https://doi.org/10.1007/978-1-4939-0802-8>.
- [38] Fischler, M. A., and Bolles, R. C., “Random Sample Consensus: A Paradigm for Model Fitting with Applications to Image Analysis and Automated Cartography,” Communications of the ACM, Vol. 24, No. 6, 1981, pp. 381–395. <https://doi.org/10.1145/358669.358692>.
- [39] Hartley, R., and Zisserman, A., Multiple View Geometry in Computer Vision, 2nd ed., Cambridge University Press 2000, UK, 2004, Chap. 3, pp. 117–120.
- [40] Carpenter, J. R., and D’Souza, C. N., “Navigation Filter Best Practices,” Tech. Rep. 20180003657, NASA, 04 2018.
- [41] Jean, I., Ng, A., and Misra, A. K., “Impact of Solar Radiation Pressure Modeling on Orbital Dynamics in the Vicinity of Binary Asteroids,” Acta Astronautica, Vol. 165, December 2019, pp. 167–183. <https://doi.org/https://doi.org/10.1016/j.actaastro.2019.09.003>.
- [42] Mortari, D., and Conway, D., “Single-Point Position Estimation in Interplanetary Trajectories Using Star Trackers,” Celestial Mechanics and Dynamical Astronomy, Vol. 128, No. 1, 2017, pp. 115–130. <https://doi.org/https://doi.org/10.1007/s10569-016-9738-4>.
- [43] Shuster, M. D., “Stellar Aberration and Parallax: A Tutorial,” The Journal of the astronautical sciences, Vol. 51, August 2003, pp. 477–494. <https://doi.org/https://doi.org/10.1007/BF03546295>.
- [44] Christian, J. A., “StarNAV: Autonomous Optical Navigation of a Spacecraft by the Relativistic Perturbation of Starlight,” Sensors, Vol. 19, No. 19, 2019, p. 4064. <https://doi.org/https://doi.org/10.3390/s19194064>.
- [45] Owen, W. M. J., “Methods of optical navigation,” Tech. Rep. 11-0589, 2011. <https://doi.org/2014/41942>.
- [46] Liu, H., Shah, S., and Jiang, W., “On-line Outlier Detection and Data Cleaning,” Computers & chemical engineering, Vol. 28, No. 9, 2004, pp. 1635–1647. <https://doi.org/https://doi.org/10.1016/j.compchemeng.2004.01.009>.
- [47] Bella, S. A., Andreis, E., Franzese, V., Panicucci, P., and Topputo, F., “Line-of-Sight Extraction Algorithm for Deep-Space Autonomous Navigation,” 2021 AAS/AIAA Astrodynamics Specialist Conference, AAS/AIAA, Virtual, August 2021.
- [48] Mamich, R., Kucharski, D., Zanetti, R., Jah, M. K., Silva, E. D., Griesbach, J. D., and Fine, J., “Navigation Using Serendipitous Star-Tracker Observations And On-Board Data Processing,” 44th AAS Guidance, Navigation and Control Conference, AAS, Breckenridge, CO, U.S.A, February 2022.

- [49] Merisio, G., Topputo, F., et al., “Characterization of Ballistic Capture Corridors Aiming at Autonomous Ballistic Capture at Mars,” 2021 AAS/AIAA Astrodynamics Specialist Conference, AAS/AIAA, Virtual, August 2022.
- [50] Yárnoz, D. G., Jehn, R., and Croon, M., “Interplanetary navigation along the low-thrust trajectory of BepiColombo,” Acta Astronautica, Vol. 59, No. 1-5, 2006, pp. 284–293. <https://doi.org/https://doi.org/10.1016/j.actaastro.2006.02.028>.
- [51] Krause, M., Thrasher, A., Soni, P., Smego, L., Isaac, R., Nolan, J., Pledger, M., Lightsey, E. G., Ready, W. J., and Christian, J., “LONESTAR: The Lunar Flashlight Optical Navigation Experiment,” arXiv preprint arXiv:2401.12198, January 2024.
- [52] Panicucci, P., and Topputo, F., “The TinyV3RSE Hardware-in-the-Loop Vision-Based Navigation Facility,” Sensors, Vol. 22, No. 23, 2022, p. 9333. <https://doi.org/https://doi.org/10.3390/s22239333>.
- [53] Pugliatti, M., Franzese, V., Panicucci, P., and Topputo, F., “TINYV3RSE: The DART Vision-Based Navigation Test-bench,” AIAA Scitech 2022 Forum, AIAA, San Diego, CA & Virtual, January 2022, p. 1193. <https://doi.org/10.2514/6.2022-1193>.
- [54] Andreis, E., Panicucci, P., Ornati, F., and Topputo, F., “Towards Validation and Verification of Autonomous Vision-Based Navigation for Interplanetary Spacecraft,” 12th International Conference on Guidance, Navigation & Control Systems (GNC), June 2023, pp. 1–14. <https://doi.org/10.5270/esa-gnc-icatt-2023-112>.
- [55] Ornati, F., Panicucci, P., Andreis, E., and Topputo, F., “RETINA: a highly-versatile optical facility for camera-in-the-loop testing of spaceborne Vision-Based Sensors,” 46th Annual AAS Guidance, Navigation and Control Conference, AAS, Breckenridge, CO, USA, February 2024.
- [56] Di Domenico, G., Andreis, E., Carlo Morelli, A., Merisio, G., Franzese, V., Giordano, C., Morselli, A., Panicucci, P., Ferrari, F., and Topputo, F., “The ERC-Funded EXTREMA Project: Achieving Self-Driving Interplanetary CubeSats,” Modeling and Optimization in Space Engineering: New Concepts and Approaches, Springer New York, 2022, pp. 167–199. https://doi.org/https://doi.org/10.1007/978-3-031-24812-2_6.
- [57] Di Domenico, G., Andreis, E., Morelli, A. C., Merisio, G., Franzese, V., Giordano, C., Morselli, A., Panicucci, P., Ferrari, F., Topputo, F., et al., “Toward self-driving interplanetary CubeSats: The ERC-funded project EXTREMA,” 72nd International Astronautical Congress, IAF, Dubai, UAE, October 2021, pp. 1–11.